CALORIMETER TECHNIQUES

Richard WIGMANS
Texas Tech University

IXth International Conference on Calorimetry
in Particle Physics
Annecy, October 9 – 14, 2000

Detection Techniques Used in Practice

- Signal generating mechanisms:
  - *Direct ionization* → *charge detection*
  - *Fluorescence* → *detection of scintillation light*
  - *Čerenkov effect* → *detection of Čerenkov light*

  !! Ionization charge and scintillation light produced by **all** charged shower particles, Čerenkov light only by the **relativistic** ones

- Calorimeters are either **homogeneous** or **sampling** the showers

- Examples of calorimeter systems used in practice:

Homogeneous ionization charge detectors:	ICARUS
Homogeneous scintillation detectors:	L3, Babar, KTeV
Homogeneous Čerenkov detectors:	OPAL, Superkamiokande
Sampling ionization charge detectors:	D0, H1 (LAr), ALEPH (gas)
Sampling scintillation detectors:	CDF, ZEUS
Sampling Čerenkov detectors:	NA50, CMS Forward

Factors determining the performance of calorimeters

- Performance = *energy resolution* **but also**
  - *signal linearity*
  - *shape of response function*
  - *time structure of signals*
  - *particle ID capability*
  - *etc.*

- Energy resolution is determined by **fluctuations**

- Fluctuations determining resolution of *electromagnetic* calorimeters:
  - Signal quantum fluctuations (*e.g.*, photoelectron statistics)
  - Sampling fluctuations
  - Shower leakage
  - Instrumental effects (*e.g.*, electronic noise, light attenuation, structural non-uniformity)

- Hadron calorimeters: The same factors play a role
  - Plus: Fluctuations in *visible energy*
  - And in most detectors: Non-compensation ($e/h \neq 1$)
    $\rightarrow$ Resolution affected by fluctuations in em shower content (π^0)
  - These additional effects usually determine the hadronic calorimeter performance

Energy resolution (em)

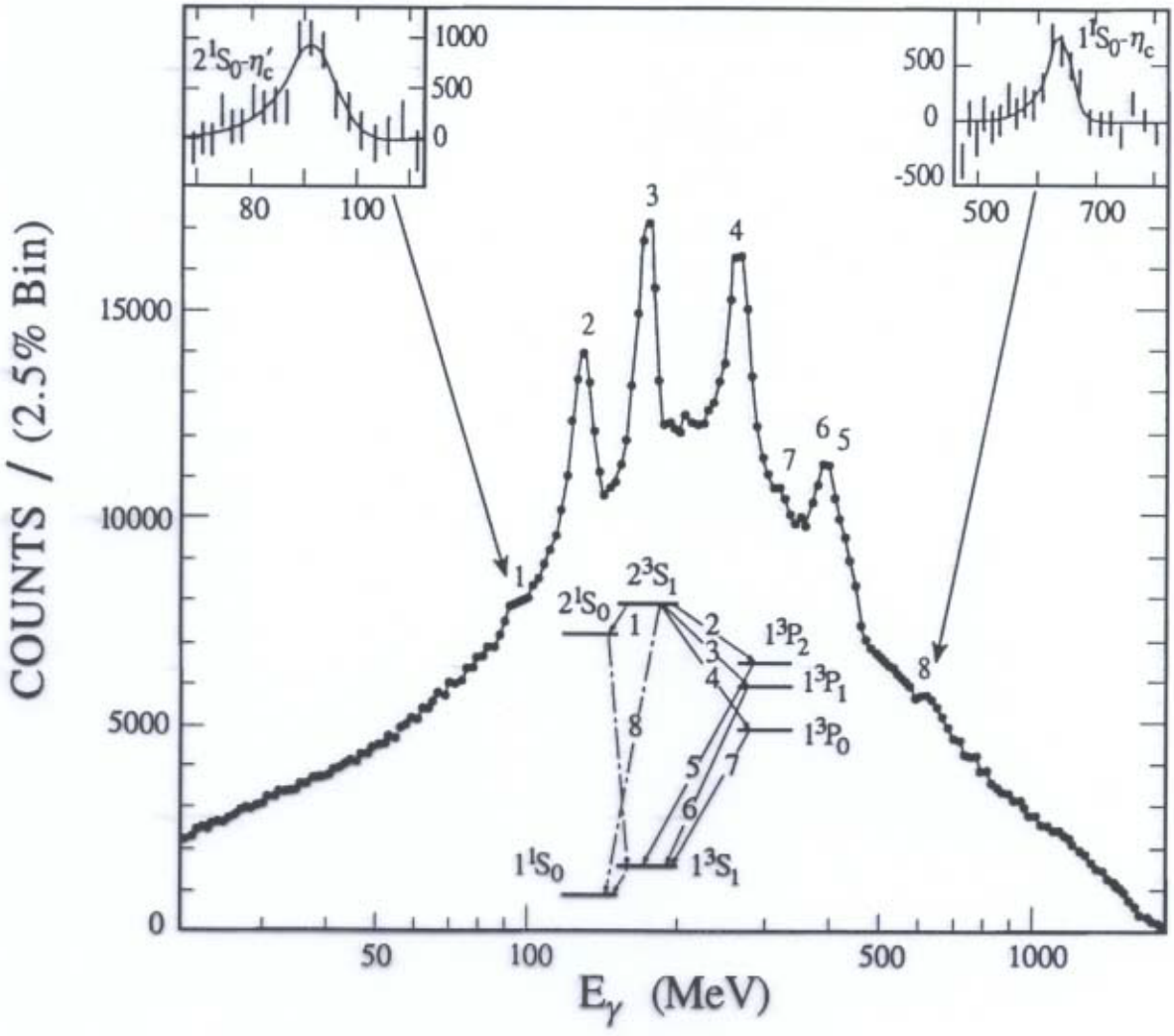

FIG. 7.2. Signal distribution for γs emitted in the radiative decay of the $\psi(2S)$, measured with the Crystal Ball NaI(Tl) calorimeter [Blo 83].

Energy resolution (em)

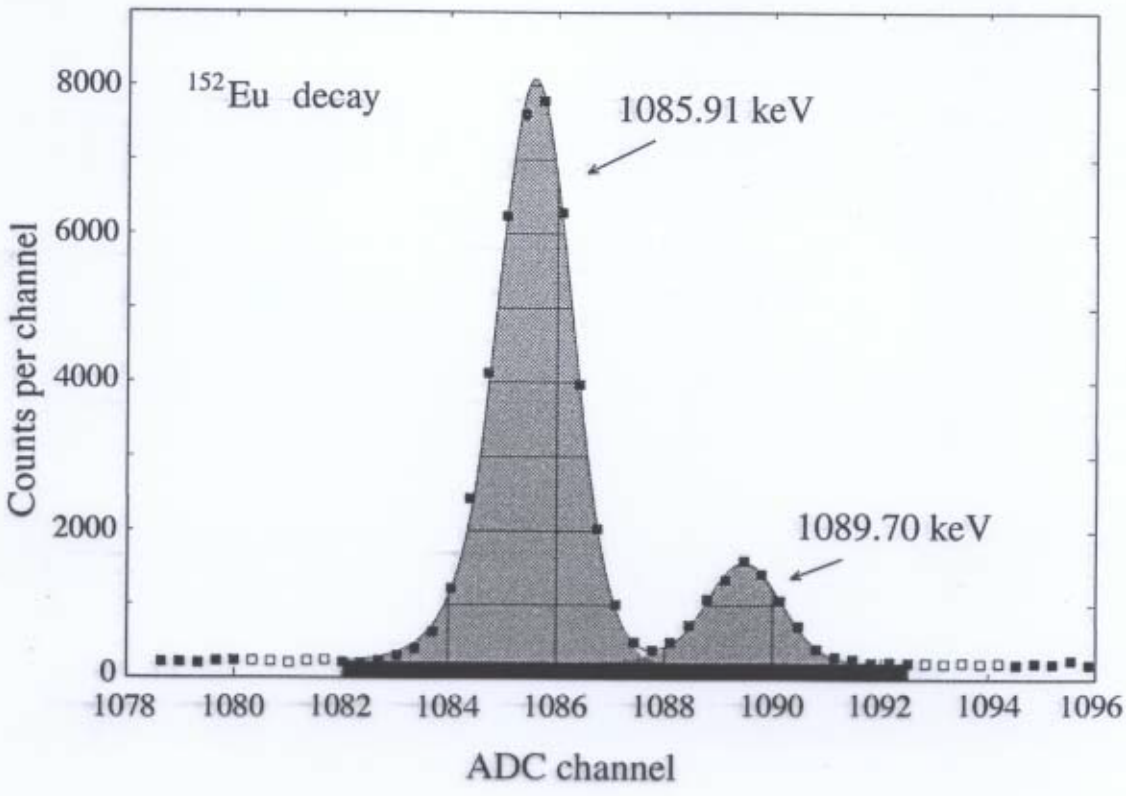

FIG. 4.1. Detection of nuclear γ-rays, from the decay of ^{152}Eu, with a high-purity germanium crystal. The energy resolution of this calorimeter is about 0.1% at 1 MeV. Courtesy of G. Roubaud, CERN.

Energy resolution (had)

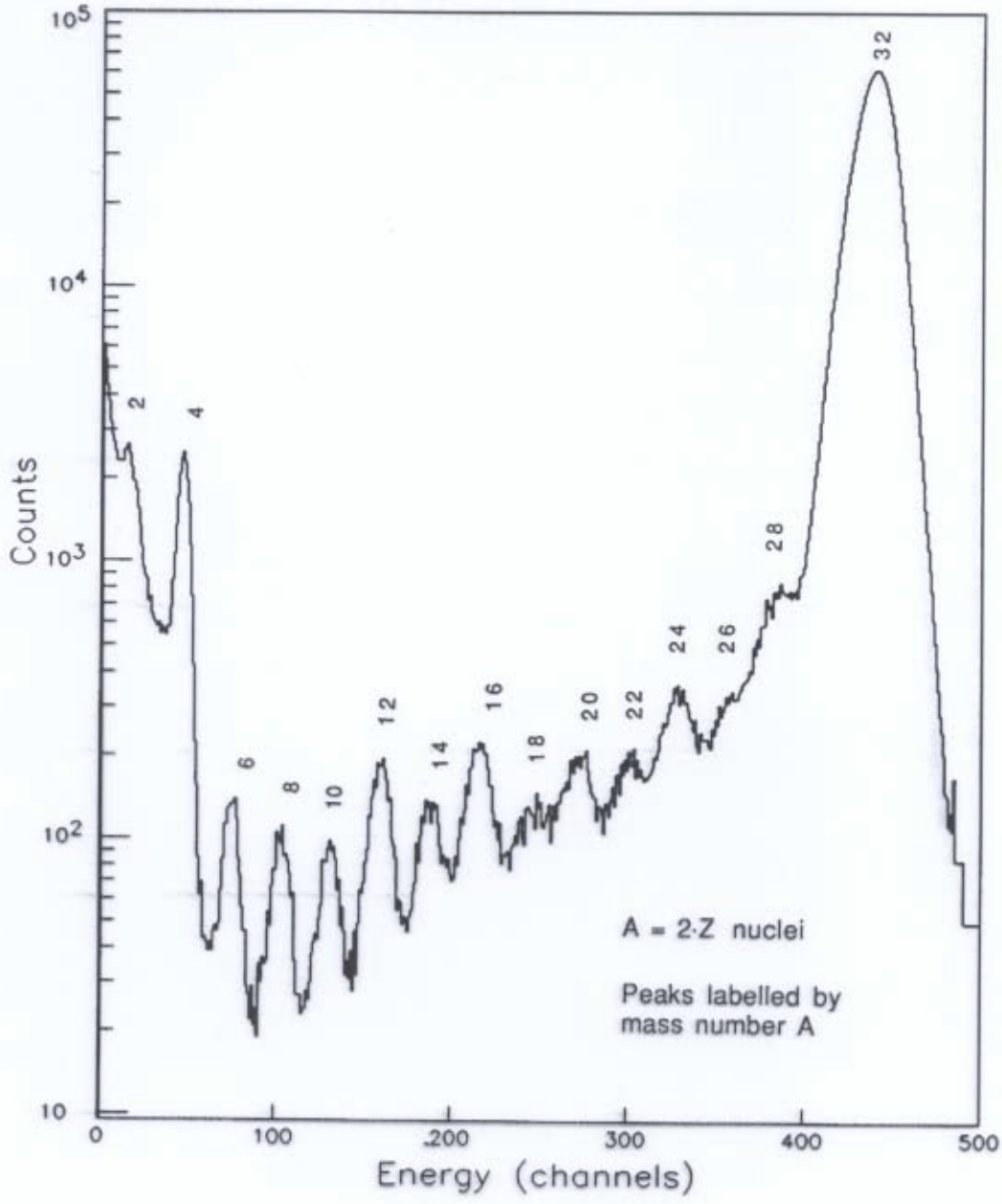

FIG. 7.51. The WA80 calorimeter as a high-resolution spectrometer. Total energy measured with the calorimeter for minimum-bias events revealed the composition of the momentum-selected CERN heavy-ion beam [You 89].

Energy resolution (had)

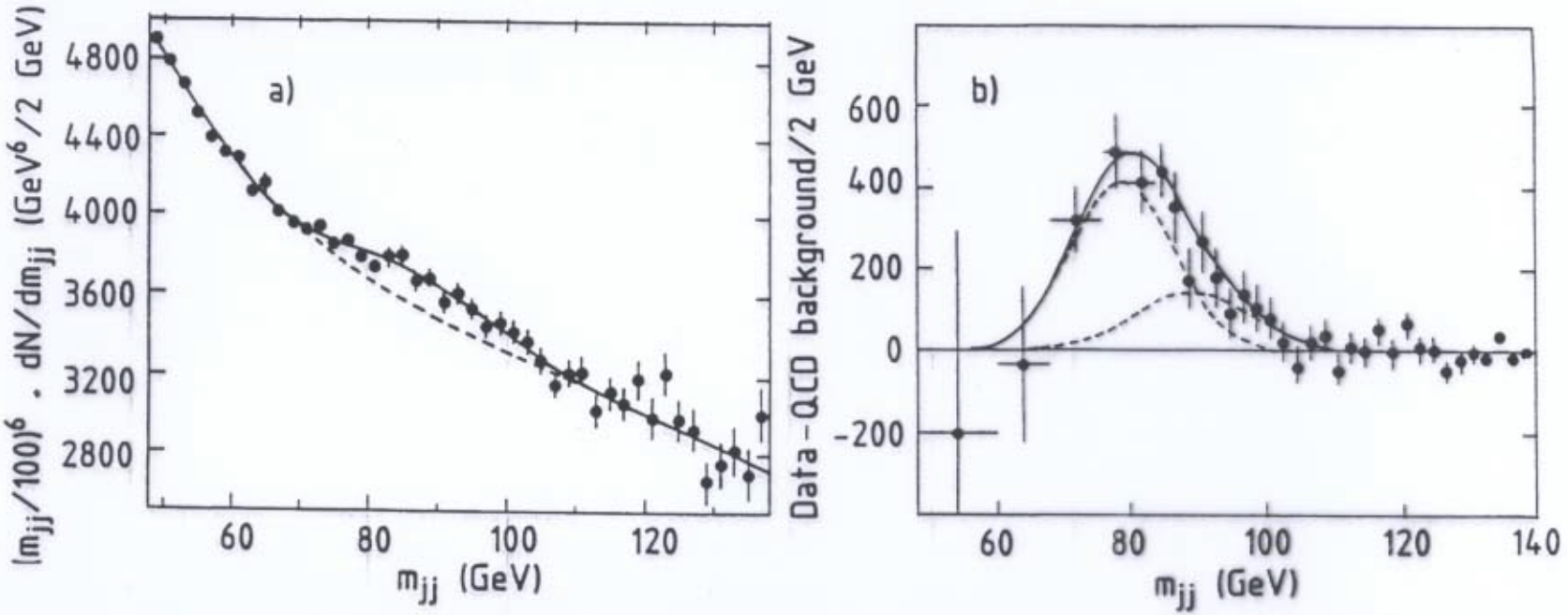

FIG. 7.50. Two-jet invariant mass distributions from the UA2 experiment [Alit 91]. Diagram *a*) shows the measured data points, together with the results of the best fits to the QCD background alone (*dashed curve*), or including the sum of two Gaussian functions describing $W, Z \rightarrow q\bar{q}$ decays. Diagram *b*) shows the same data after subtracting the QCD background. The data are compatible with peaks at $m_W = 80$ GeV and $m_Z = 90$ GeV. The measured width of the bump, or rather the standard deviation of the mass distribution, was 8 GeV, of which 5 GeV could be attributed to non-ideal calorimeter performance [Jen 88].

Fluctuations

- *Energy dependence* is not the same for different types of fluctuations
  - Poissonian (*e.g.*, sampling, signal quantum): $\sigma/E \sim E^{-1/2}$
  - Electronic noise: $\sigma/E \sim E^{-1}$
  - Light attenuation: $\sigma/E =$ constant
  - Longitudinal shower leakage: σ/E increases with energy

$\Rightarrow$ Relative importance of the effects contributing to the energy resolution depends on the energy

$\Rightarrow$ At high energies, non-stochastic effects dominate

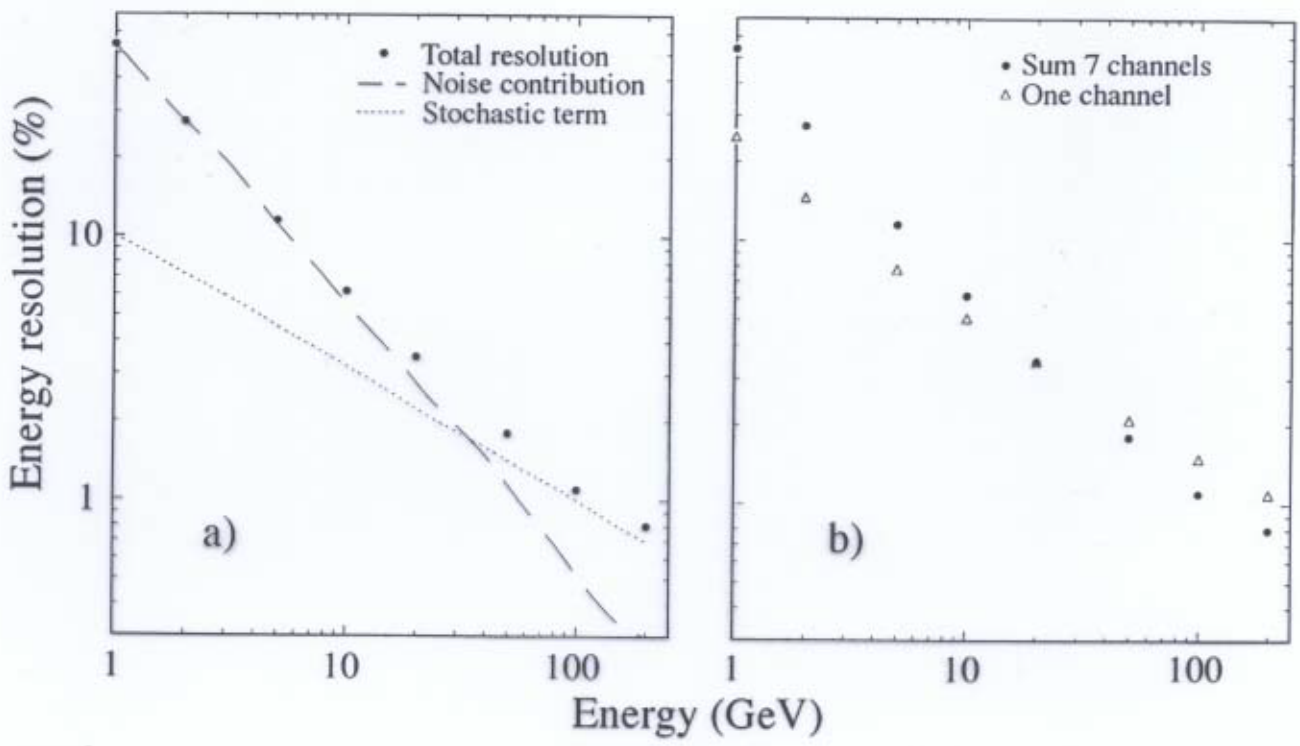

FIG. 4.16. The energy resolution and its contributing terms for a liquid-argon calorimeter of which the properties are described in the text.

1 cell : $\sigma/E = \frac{15\%}{\sqrt{E}} \oplus \frac{0.2}{E}$

7 cells : $\sigma/E = \frac{10\%}{\sqrt{E}} \oplus \frac{0.2\sqrt{7}}{E}$

Fluctuations and calorimeter design

- *Improve* resolution → work on fluctuations that **dominate**.
  Example: 60 ton liquid scintillator calorimeter .
  (**All** fluctuations eliminated, except non-compensation):
  $\sigma/E > 10\%$ at all energies!
  SPACAL ($e/h \approx 1.0$, but other sources of fluctuation present):
  $\sigma/E \approx 2\%$ at $E = 300$ GeV

- Do not spend your money reducing fluctuations that do **not** dominate. Examples:

  - A $2\lambda_{\text{int}}$ deep calorimeter for extraterrestrial detection of high energy cosmic hadrons is dominated by *shower leakage*
    → A high-quality crystal calorimeter is as good (bad) as a crudely sampling one

  - A calorimeter system with a crystal em section will have poor performance for hadron detection, *no matter what* you choose as the hadronic section, because of the large e/h value of homogeneous devices
    → *Don't waste your money on the hadronic section*

  - The light yield of quartz fiber calorimeters is so small that signal quantum fluctuations (photoelectron statistics) are an important contribution to the resolution
    → There is typically nothing to be gained by making a finer-sampling detector (more, thinner fibers instead of fewer, thicker ones)

Hadron showers
Effect of fem fluctuations on resolution

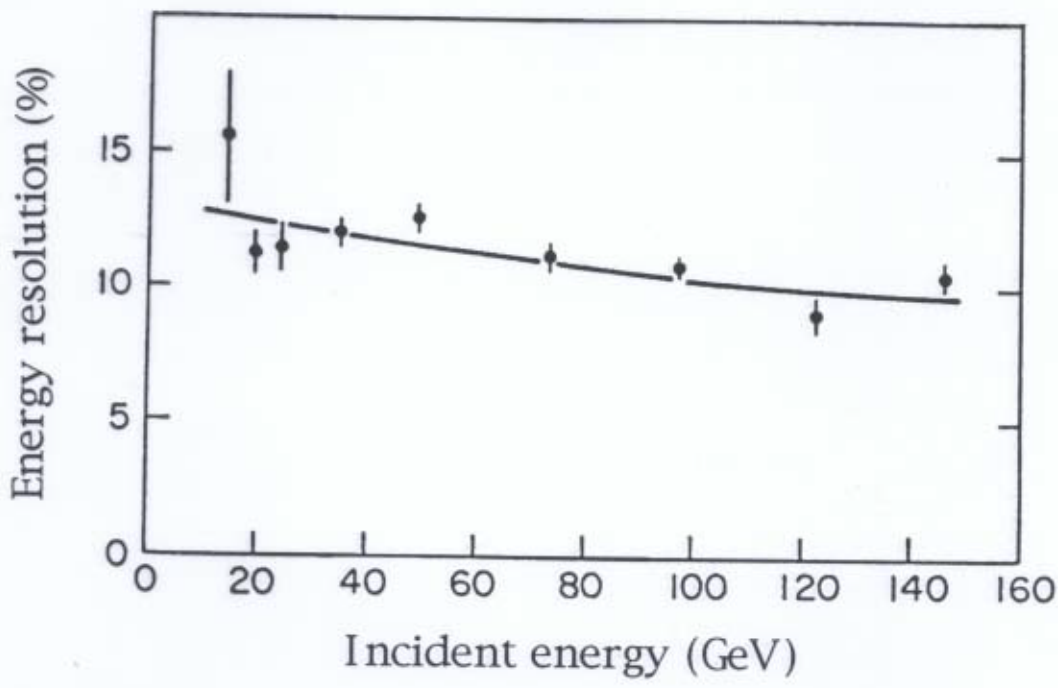

Figure 9: The hadronic energy resolution as a function of energy, for a homogeneous calorimeter consisting of 60 tonnes of liquid scintillator[18]

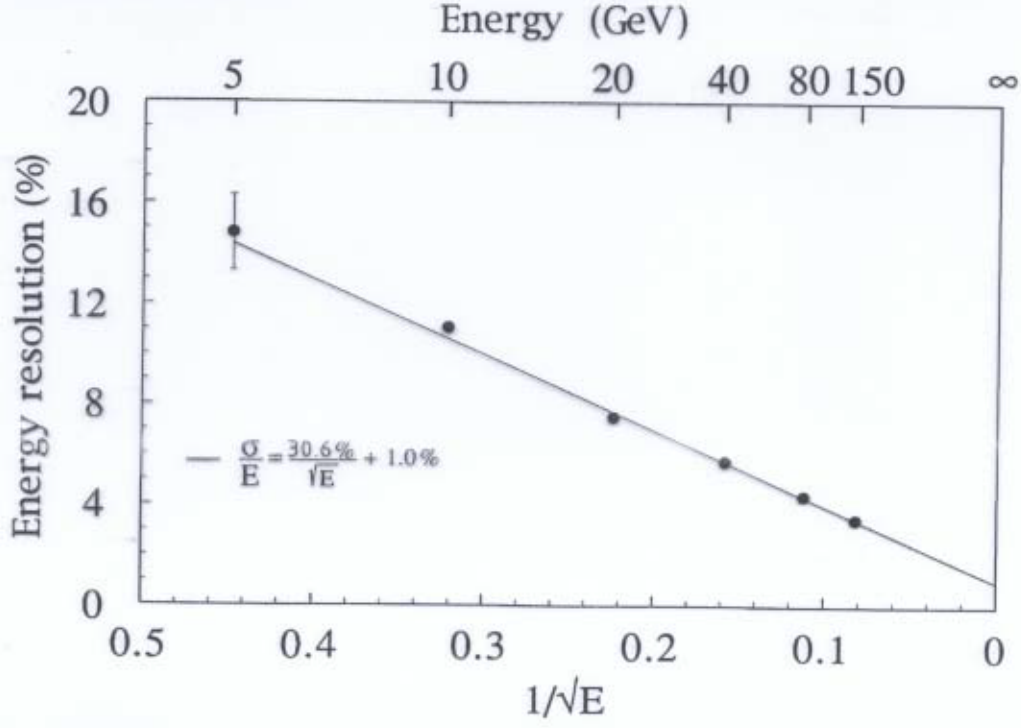

Figure 10: The hadronic energy resolution as a function of energy, for the compensating

Hadron showers in ACCESS

(1.4 λ_{int} prototype)

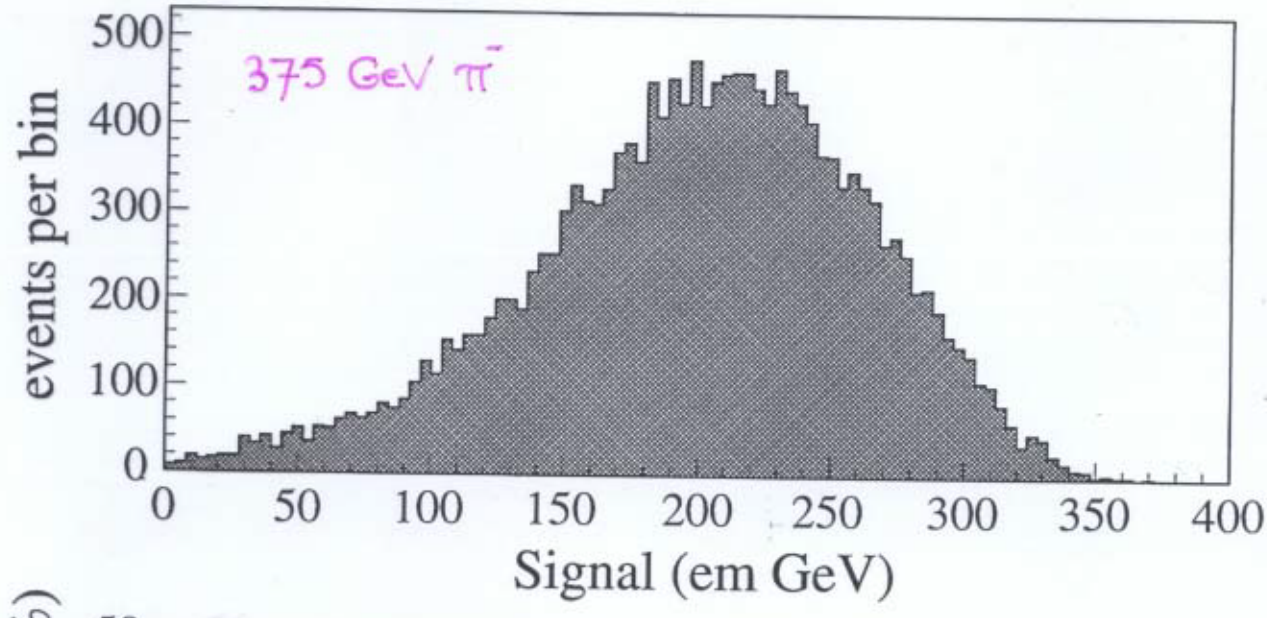

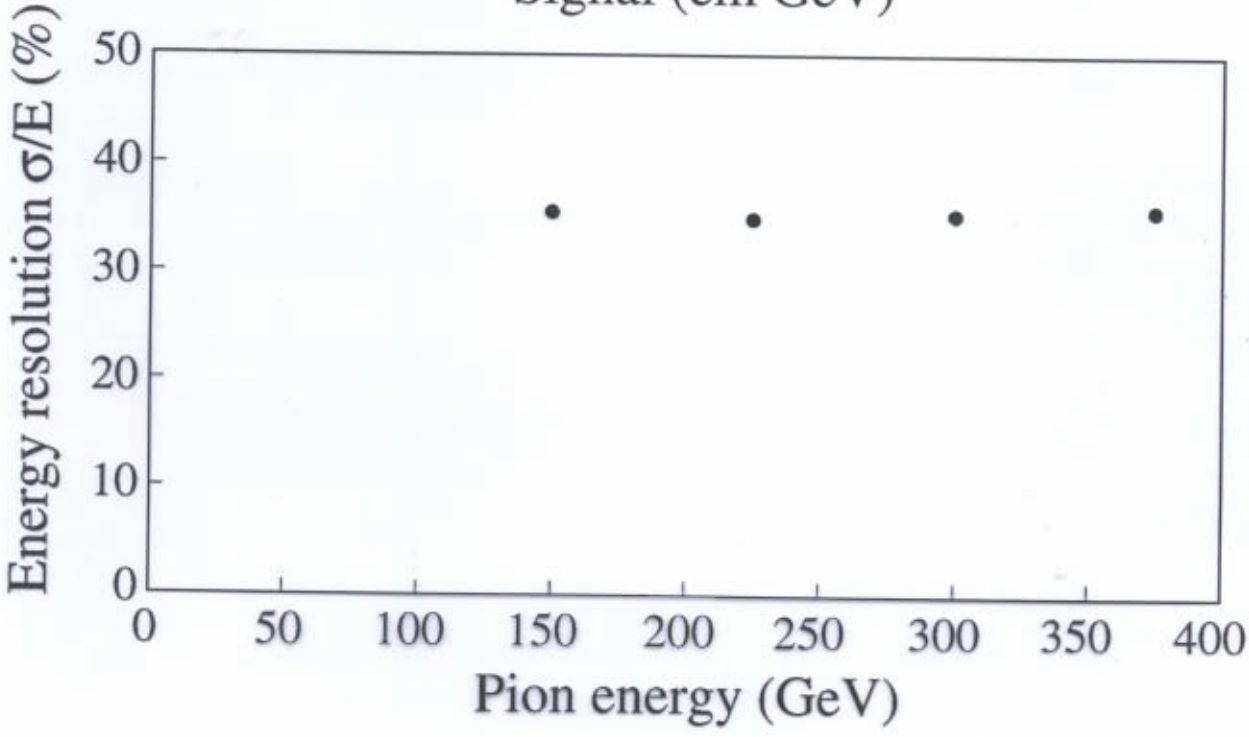

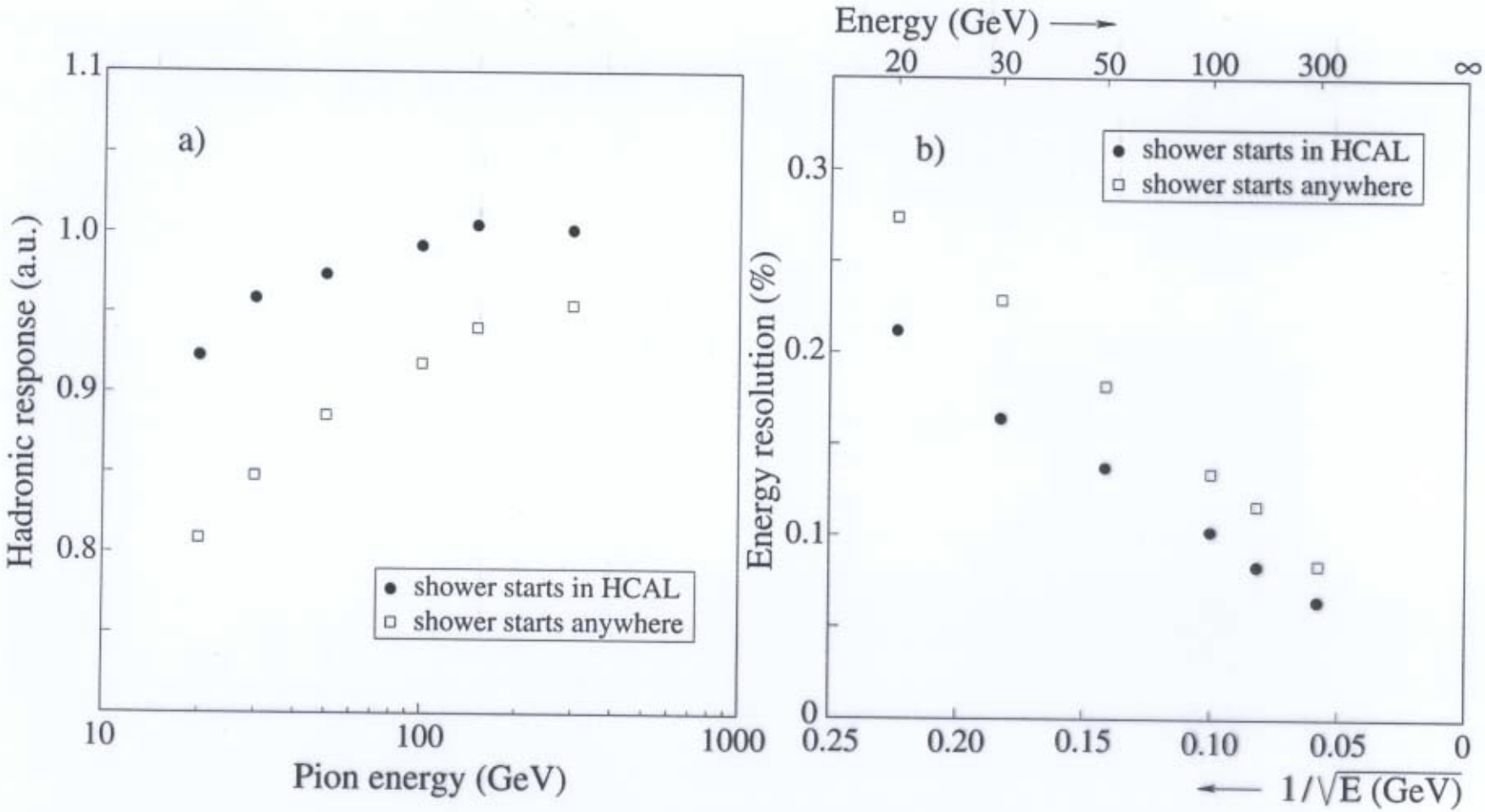

FIG. 8.17. Experimental results for pion detection in a prototype of the CMS calorimeter system. Shown are the response (*a*) and the energy resolution (*b*), as a function of the pion energy. The open squares represent the experimental results for all events; the full dots were obtained for events in which the starting point of the showers was located in the hadronic calorimeter section [Deb 97].

Signal quantum fluctuations

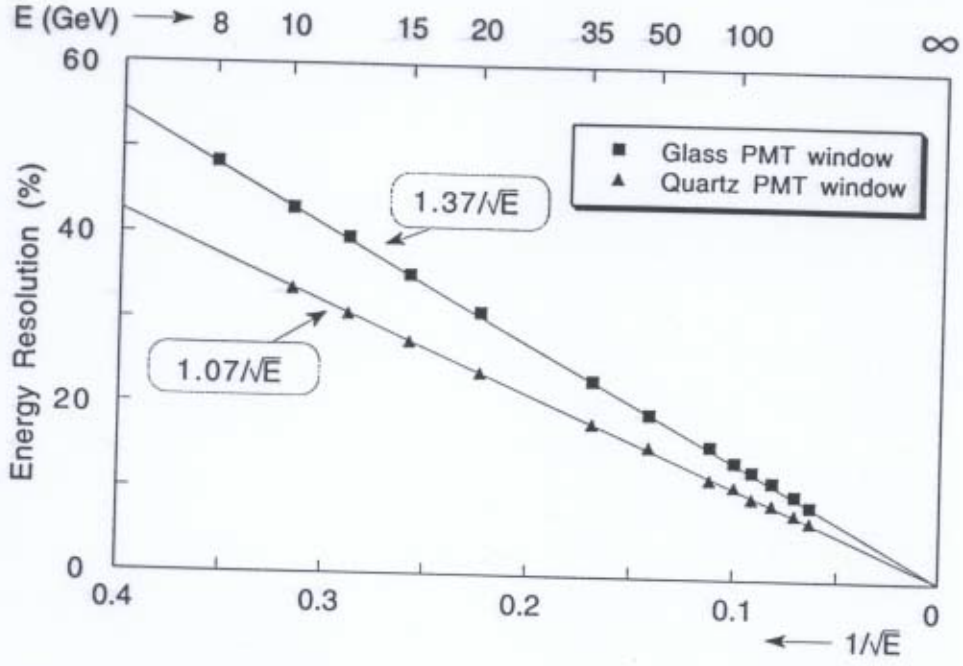

FIG. 4.2. The energy resolution for electron detection with the QFCAL prototype detector, as a function of energy. Results are given for measurements in which photomultiplier tubes with a glass window were used and for measurements in which the same type of PMTs were equipped with a quartz window [Akc 97].

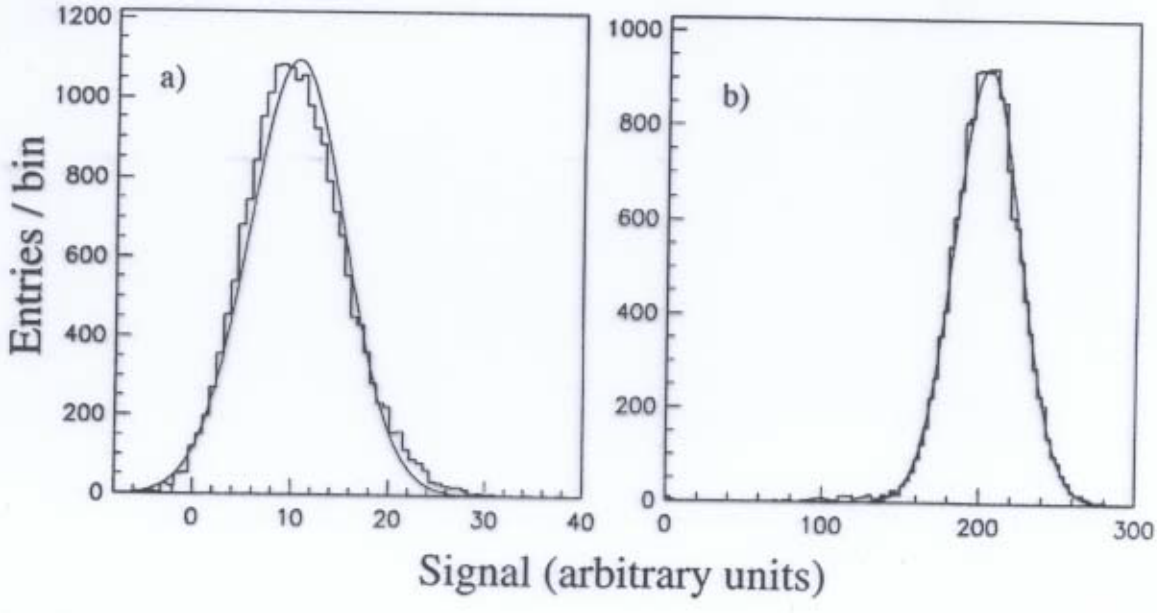

FIG. 4.3. Signal distributions for 10 GeV (*a*) and 200 GeV (*b*) electrons showering in the CMS Quartz-Fiber calorimeter, measured with a PMT with a glass window. The curves represent Gaussian fits to the experimental data [Akc 97].

Sampling fluctuations (em)

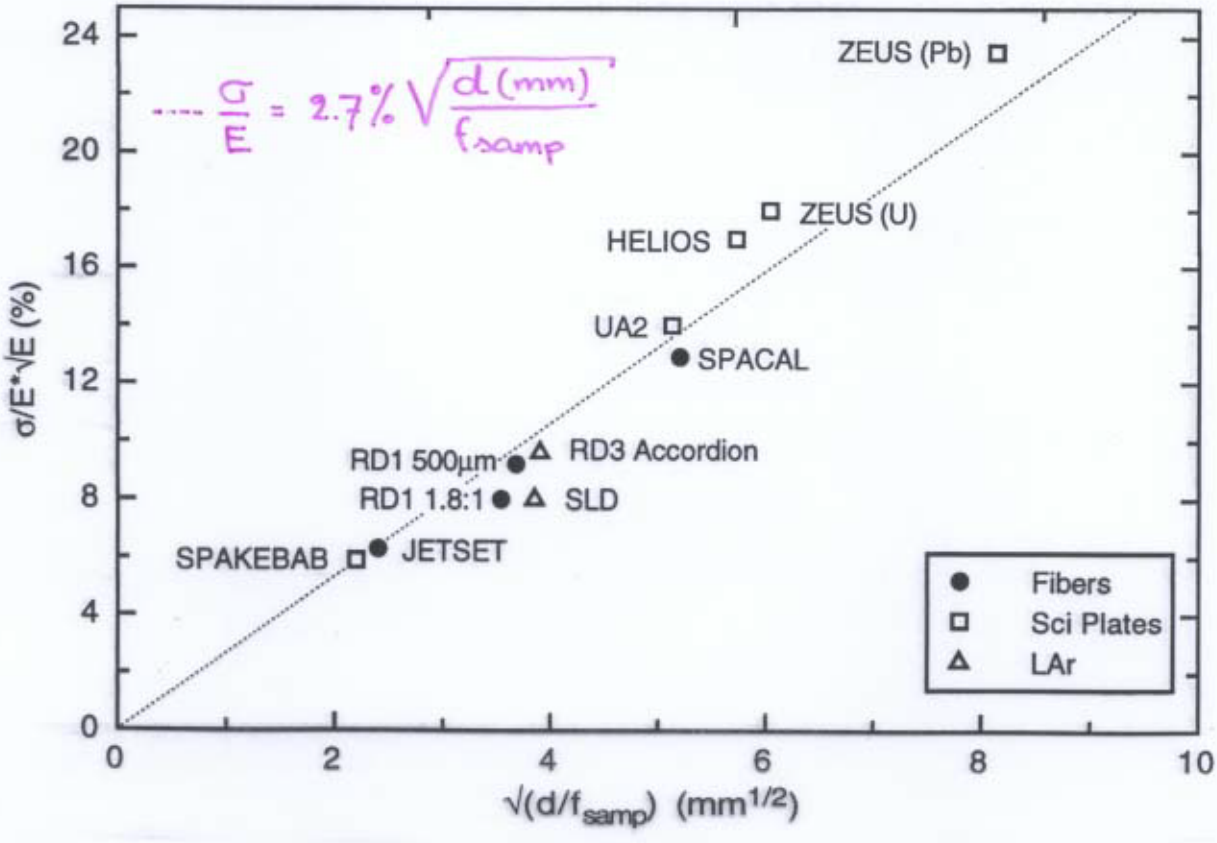

FIG. 4.8. The em energy resolution of sampling calorimeters as a function of the parameter $(d/f_{\text{samp}})^{1/2}$, in which d is the thickness of an active sampling layer (*e.g.* the diameter of a fiber or the thickness of a scintillator plate or a liquid-argon gap), and f_{samp} is the sampling fraction for mips [Liv 95].

Shower leakage fluctuations (em)

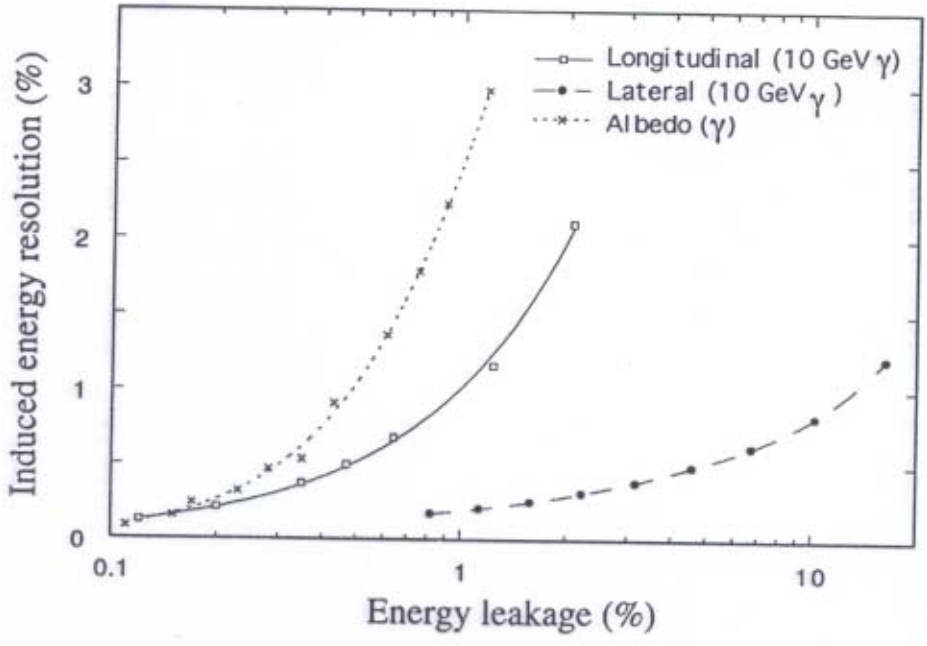

FIG. 4.37. A comparison of the effects caused by different types of shower leakage. Shown are the induced energy resolutions resulting from albedo, longitudinal and lateral leakage as a function of the average energy fraction carried by particles escaping from the detector. The longitudinal and lateral leakage data concern 10 GeV γs, the albedo data are for γ-induced showers of different energies. Results from EGS4 Monte Carlo calculations.

Fluctuations due to instrumental effects
(structural non-uniformity)

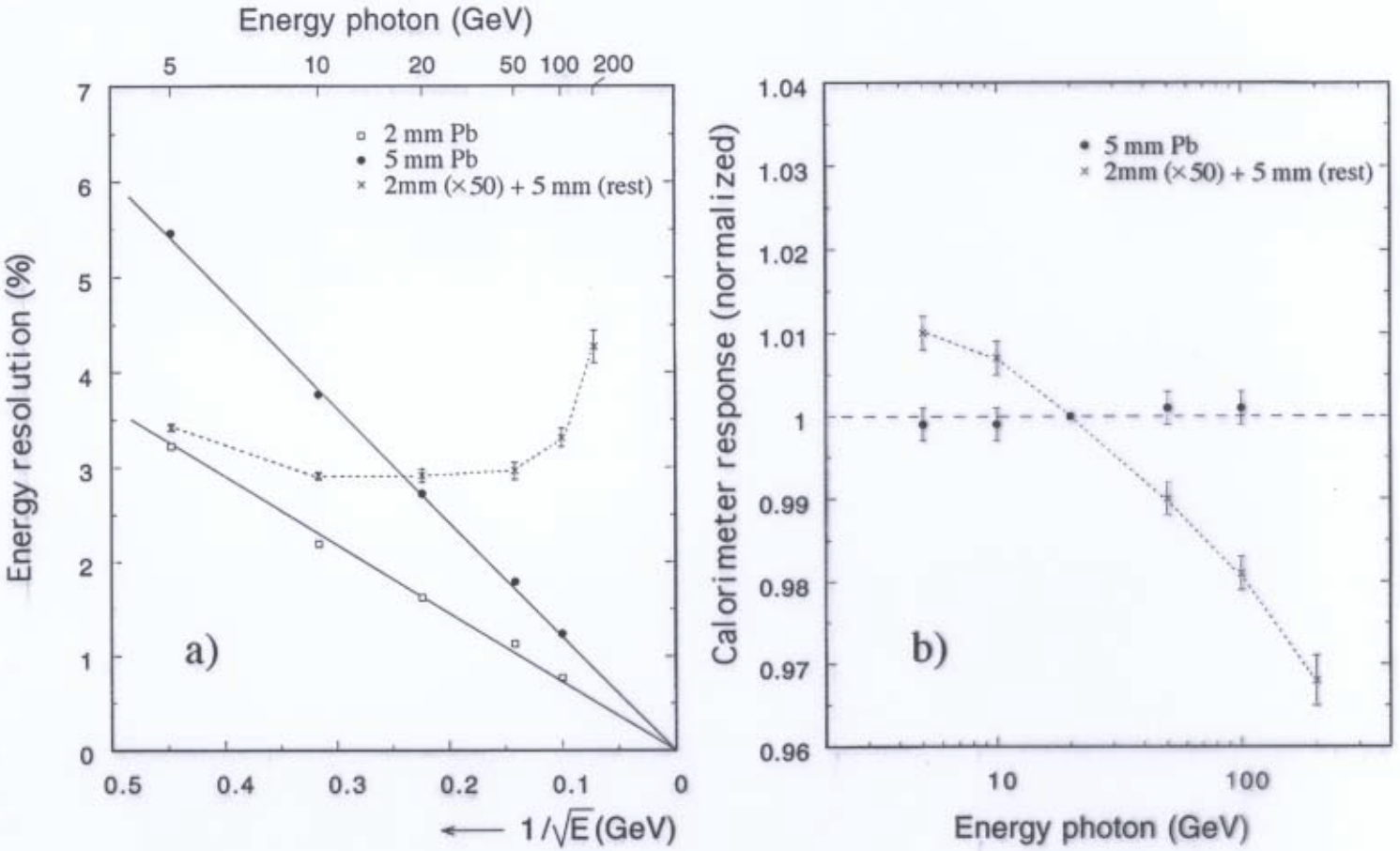

FIG. 4.20. The energy resolution (*a*) and the response (*b*) as a function of energy, for high-energy γs showering in three different Pb/scintillator calorimeters, all equipped with 2.5 mm thick scintillator plates. Detector 1 uses 2 mm thick lead plates. Detector 2 uses 4 mm thick lead plates. Detector 3 contains fifty 2 mm thick lead plates, followed by 5 mm thick lead plates in the rest of the device. Results from EGS4 Monte Carlo simulations.

(readout)

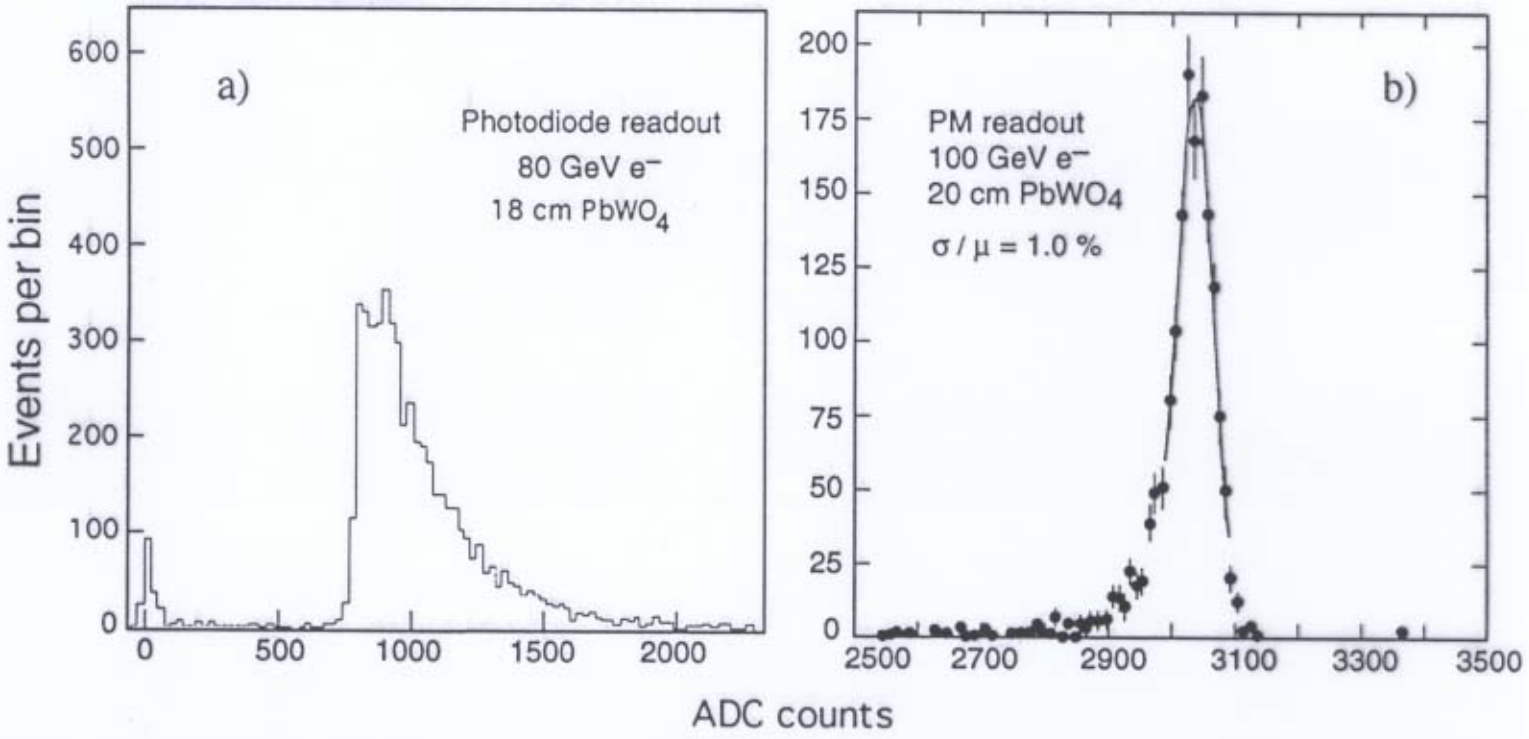

FIG. 3.3. Signal distributions for high-energy electron showers measured with a prototype $PbWO_4$ crystal calorimeter. The calorimeter was read out either with silicon photodiodes (*a*) or with photomultiplier tubes (*b*). Data from [Pei 96].

Fluctuations in Hadron Calorimetry

- π^0 production in hadron absorption $\rightarrow$ em showers (em fraction $f_{\rm em}$).
  Non-em fraction: ionization by $\pi^{\pm}$, p.
  Nuclear binding energy losses $\rightarrow$ fluctuations in *visible* energy.
  In general, response to em shower component larger than to non-em ($e/h > 1$).

- $\langle f_{\rm em} \rangle$ increases with energy $\rightarrow$ hadronic signal non-linearity.
  (At low energy non-linearity because of $e/mip \neq 1$).

- Fluctuations in $f_{\rm em}$ are large and non-Gaussian $\rightarrow$ affect line shape.
  Fluctuations are different for proton, pion showers (leading-π^0 effect).

- Sampling fraction for soft neutrons may be much larger than for charged shower particles (hydrogen!) $\rightarrow$ **compensation** ($e/h = 1$).

- Effect of non-compensation on resolution is **not** $\oplus$ constant.

- Fluctuations in neutron signals may be huge (Texas tower effect).

- Compensation eliminates effects of *event-to-event* $f_{\rm em}$ *fluctuations*.
  This can **not** be achieved with global weighting factors aiming for $e/\pi = 1$.

Energy deposit in hadron showers

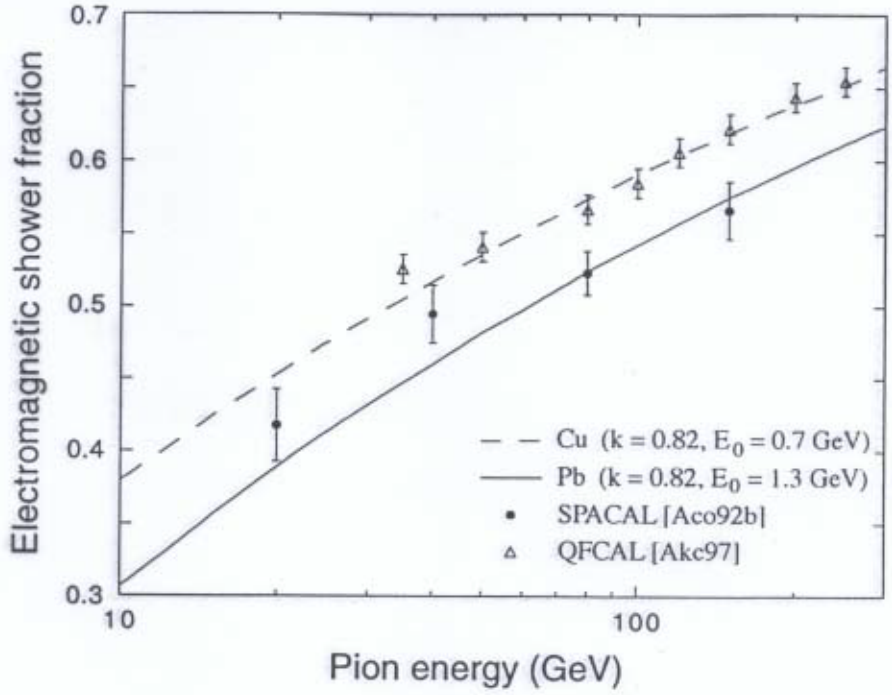

FIG. 2.22. Comparison between the experimental results on the em fraction of pion-induced showers in the (copper-based) QFCAL and (lead-based) SPACAL detectors. Data from [Akc 97] and [Aco 92b].

Table 2.5 *Energy deposit and composition of the non-em component of hadronic showers in lead and iron. The listed numbers of particles are per GeV of non-em energy.*

	Lead	*Iron*
Ionization by pions	19%	21%
Ionization by protons	37%	53%
Total ionization	56%	74%
Nuclear binding energy loss	32%	16%
Target recoil	2%	5%
Total invisible energy	34%	21%
Kinetic energy evaporation neutrons	10%	5%
Number of charged pions	0.77	1.4
Number of protons	3.5	8
Number of cascade neutrons	5.4	5
Number of evaporation neutrons	31.5	5
Total number of neutrons	36.9	10
Neutrons/protons	10.5/1	1.3/1

Energy deposit in hadron showers

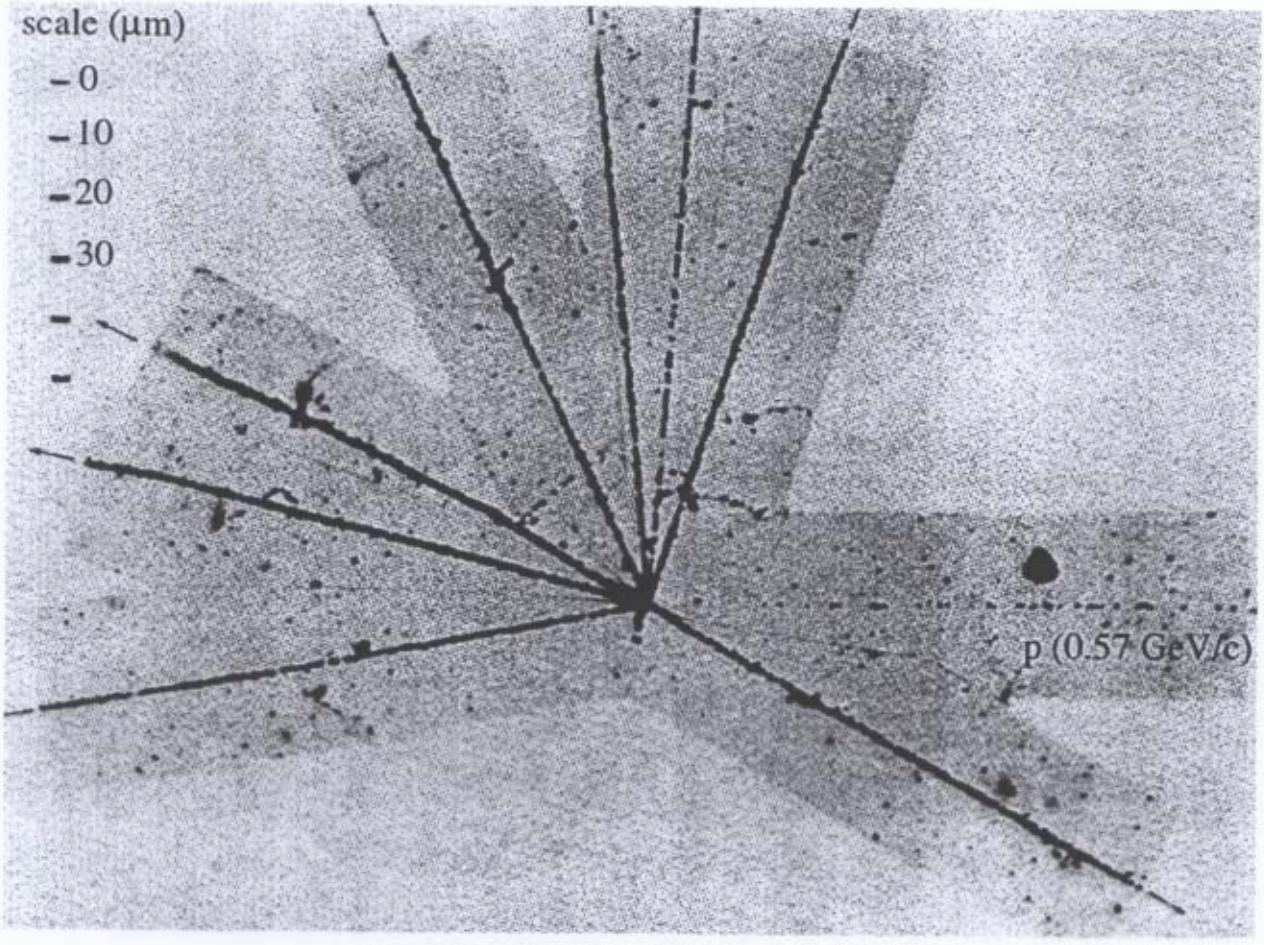

FIG. 2.42. A nuclear interaction induced by a proton with a kinetic energy of 160 MeV in a nuclear emulsion stack. Photograph courtesy CERN.

Hadronic signal non-linearity
effects of e/h and e/mip

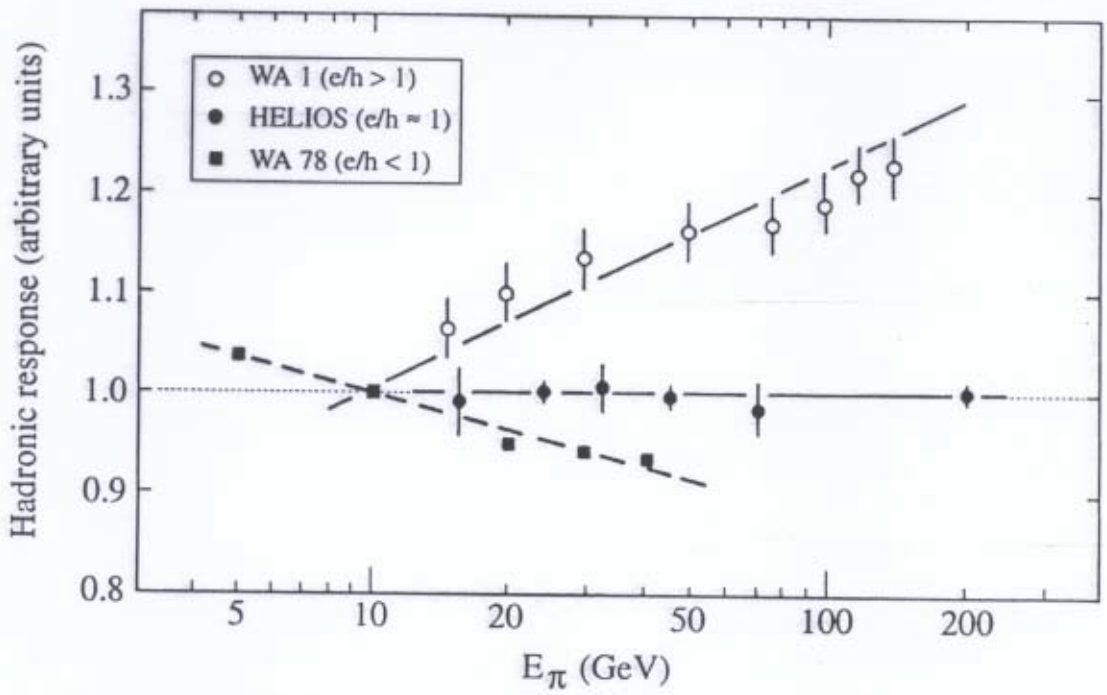

FIG. 3.14. The response to pions as a function of energy for three calorimeters with different e/h values: the WA1 calorimeter ($e/h > 1$, [Abr 81]), the HELIOS calorimeter ($e/h \approx 1$, [Ake 87]) and the WA78 calorimeter ($e/h < 1$, [Dev 86, Cat 87]). All data are normalized to the results for 10 GeV.

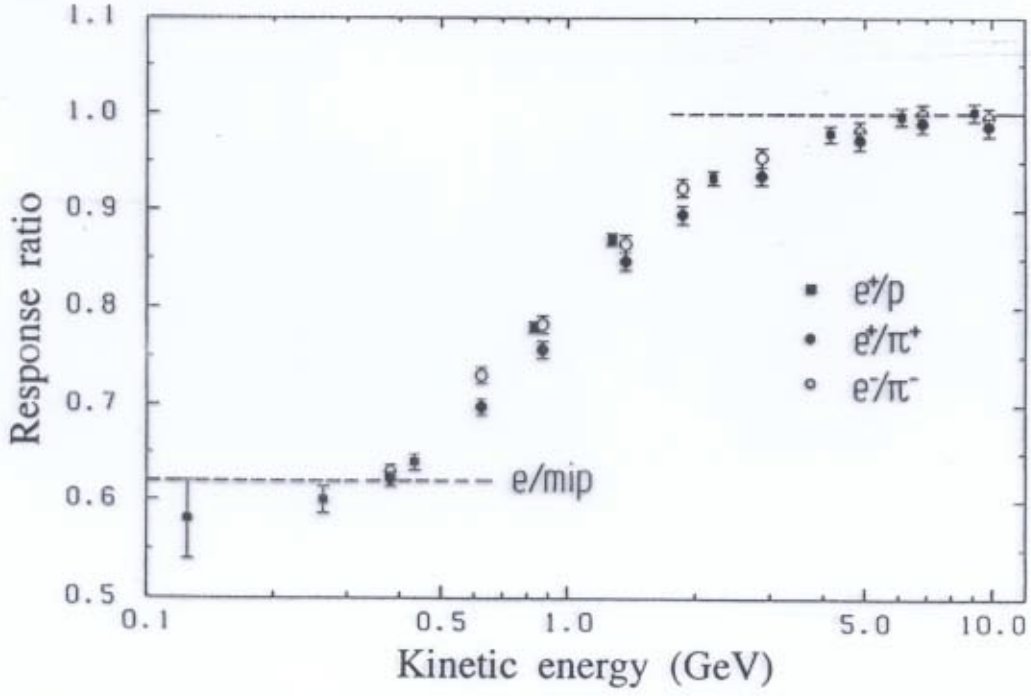

FIG. 3.13. The response of the (compensating) ZEUS calorimeter to low-energy hadrons. Data from [And 90].

Hadronic response function (π)

effect of e/h

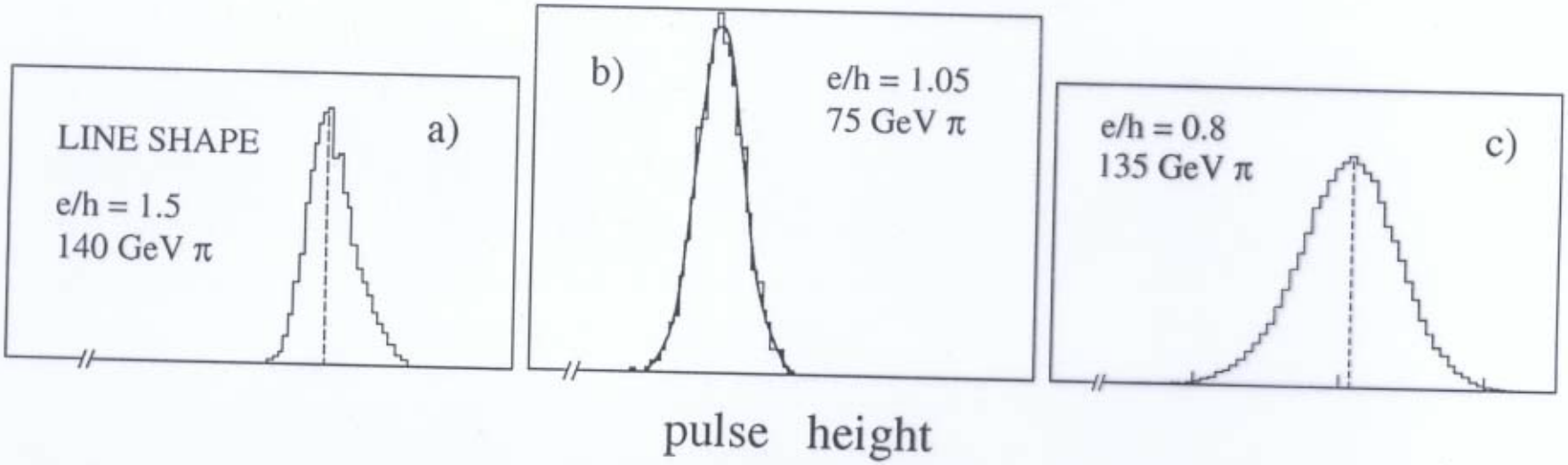

FIG. 7.24. Signal distributions for mono-energetic pions in calorimeters with different e/h values. Data from WA1 [Abr 81], ZEUS [Beh 90] and WA78 [Dev 86].

Fluctuations in em shower component fem
proton/pion differences

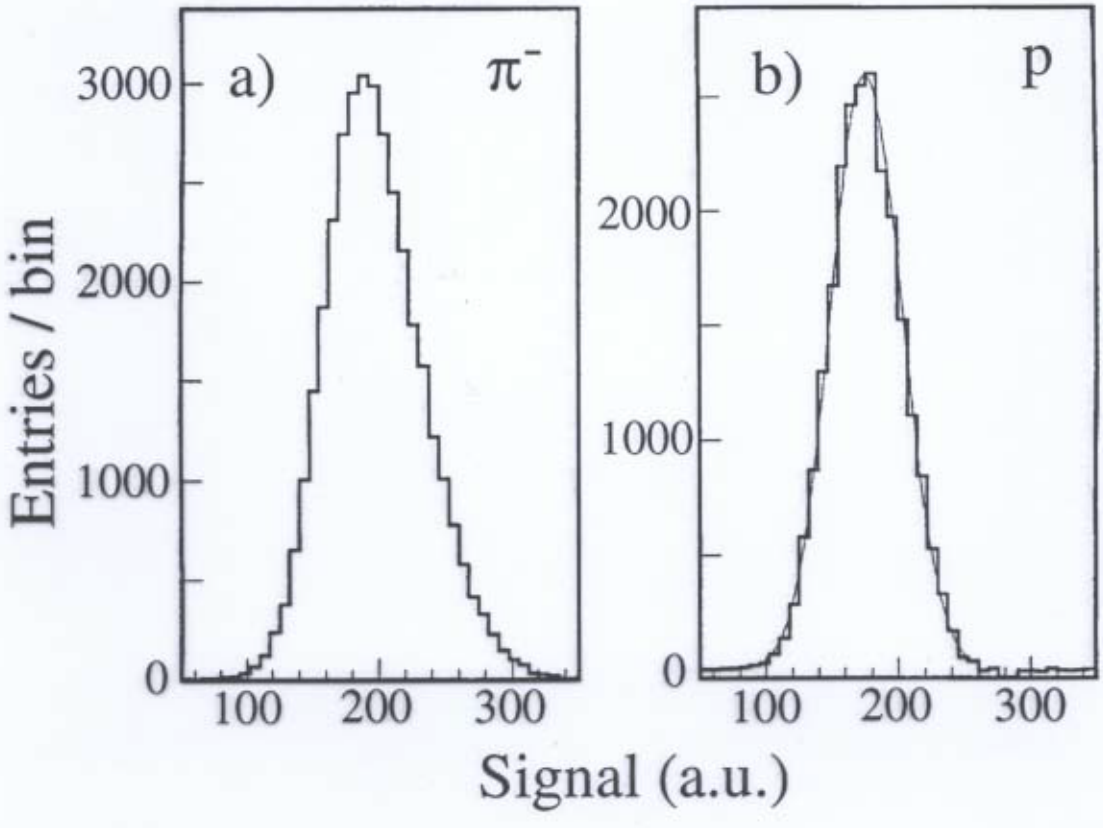

FIG. 4.49. Signal distributions for 300 GeV pions (*a*) and protons (*b*) detected with a quartz-fiber calorimeter. The curve represents the result of a Gaussian fit to the proton distribution [Akc 98].

Compensation in gas calorimeters

Response for different gases

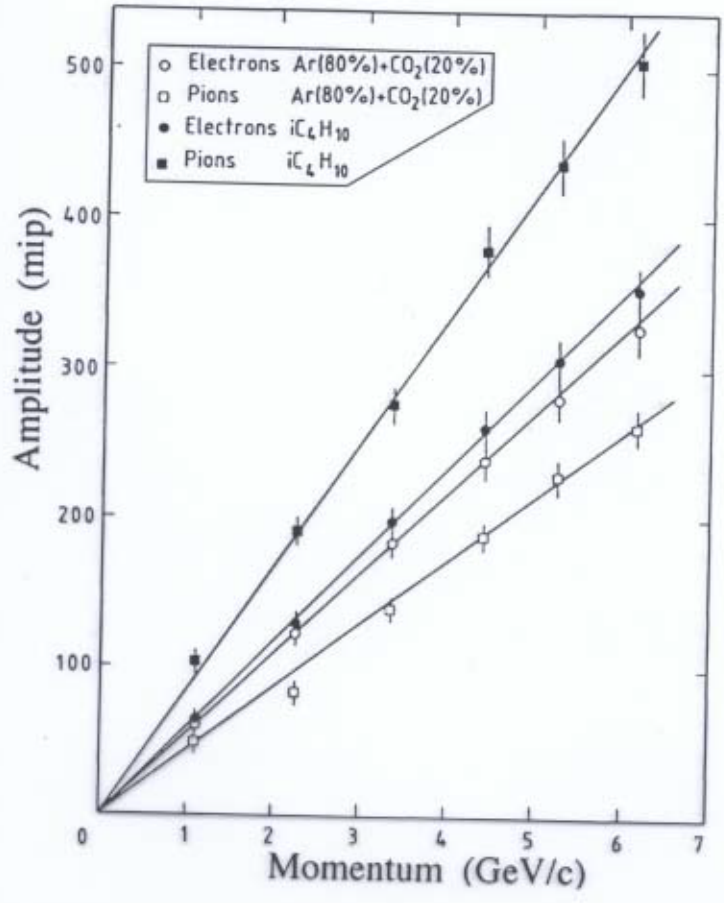

FIG. 3.31. The average signals for electrons and pions, measured with the uranium/gas calorimeter of the L3 Collaboration, for two different choices of gas with which the proportional wire chambers were operated [Gal 86].

Compensation in Pb/scintillator calorimeters:
effect of sampling fraction on e/h

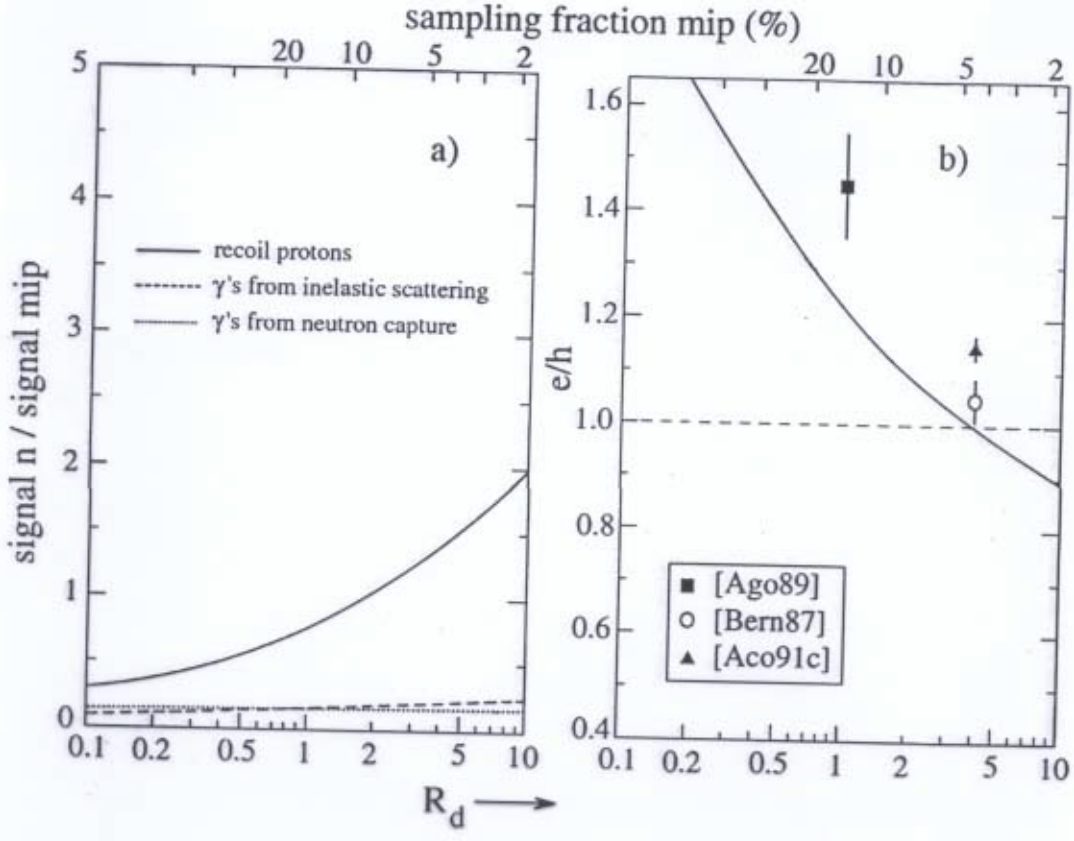

FIG. 3.34. The n/mip response ratio, split up into its components, for Pb/PMMA calorimeters, as a function of R_d, the ratio of the thicknesses of the passive and active calorimeter layers (a). The e/h ratio as a function of R_d (b). The top axis of both graphs indicates the sampling fraction for mips. From [Wig 87].

Compensation in Pb/scintillator calorimeter

effect of sampling fraction on e/π

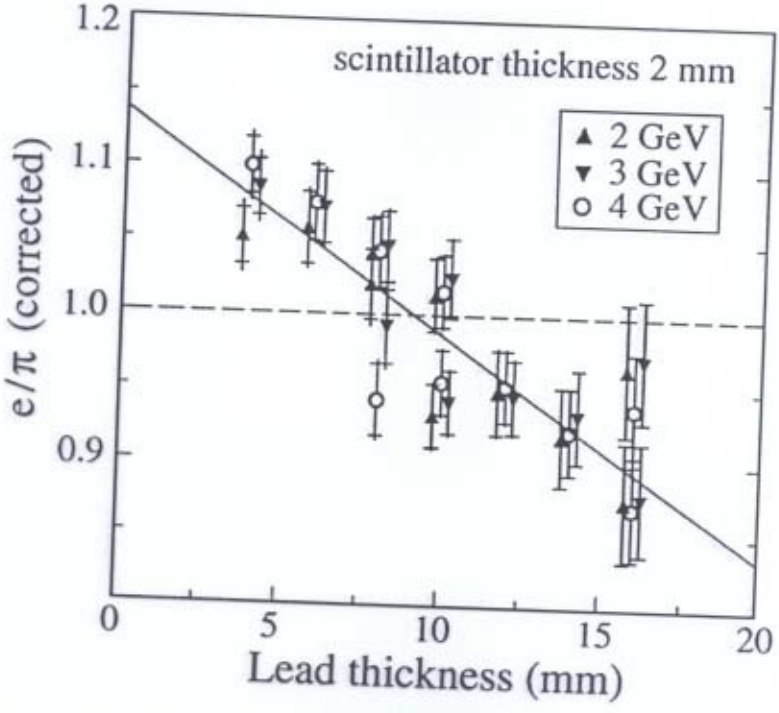

FIG. 3.35. The e/π signal ratio, corrected for the effects of shower leakage, for lead/polystyrene-scintillator calorimeters, as a function of the thickness of the lead plates, for 2 mm thick scintillator plates. The inner (outer) error bars show the combined systematic and statistical uncertainty without (with) the shower leakage corrections. The line in the plot is a result of a linear fit to the experimental data [Suz 99].

Compensation in Pb/scintillator calorimeter

effect on hadronic energy resolution

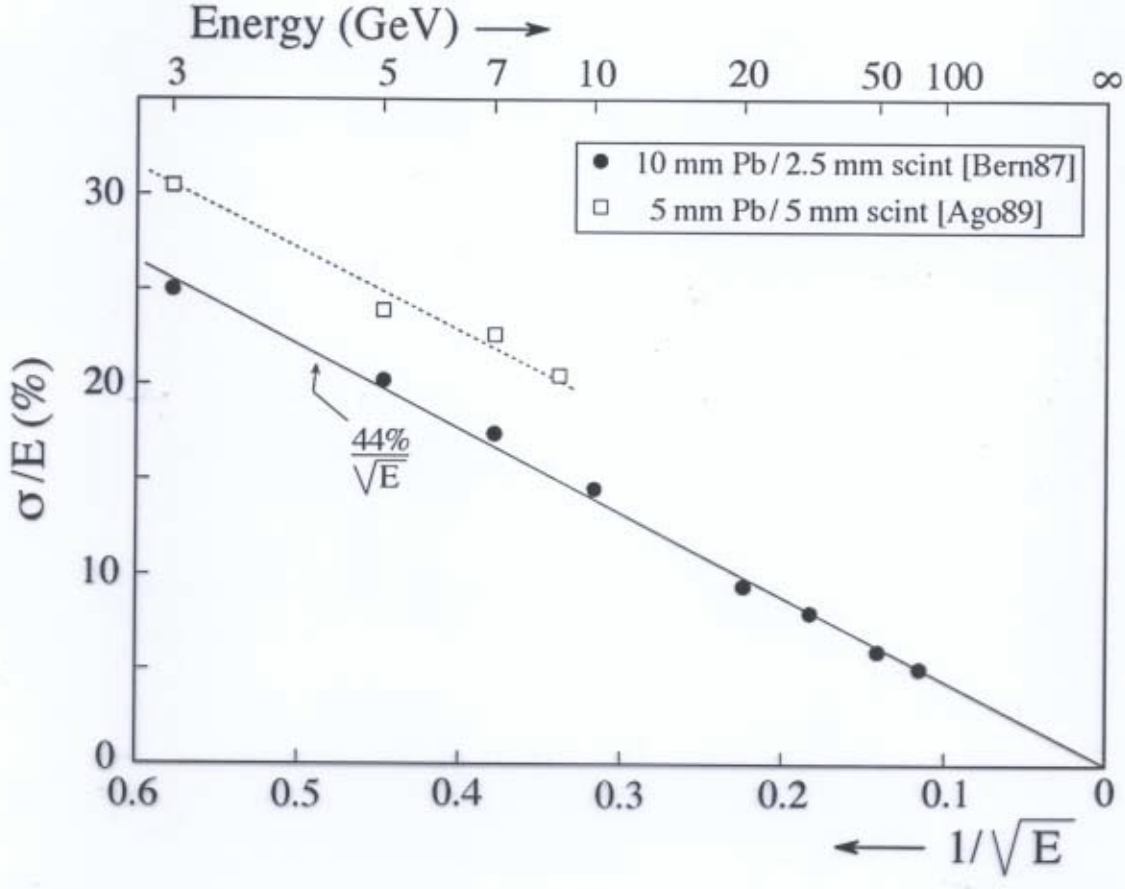

FIG. 8.1. The hadronic energy resolution as a function of energy, for two different Pb/scintillator calorimeter prototypes built and tested by the ZEUS Collaboration. Data from [Ago 89] and [Bern 87].

Energy resolution of a non-compensatir calorimeter (π)

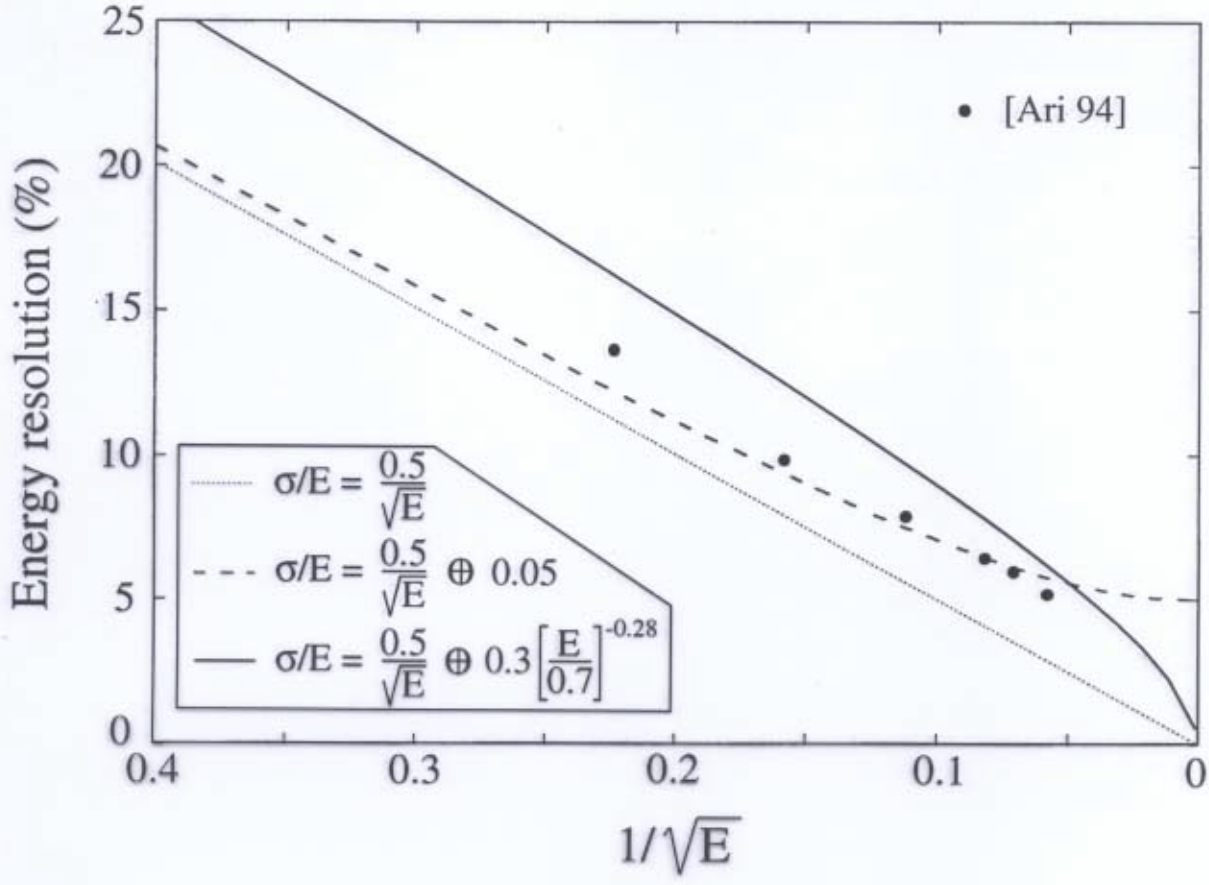

FIG. 4.47. Comparison between Equations 4.28 (the dashed curve) and 4.29 (the solid curve). The dotted line represents the stochastic term in these equations. The experimental data were taken from [Ari 94]. See text for details.

Energy resolution of a non-compensating calori

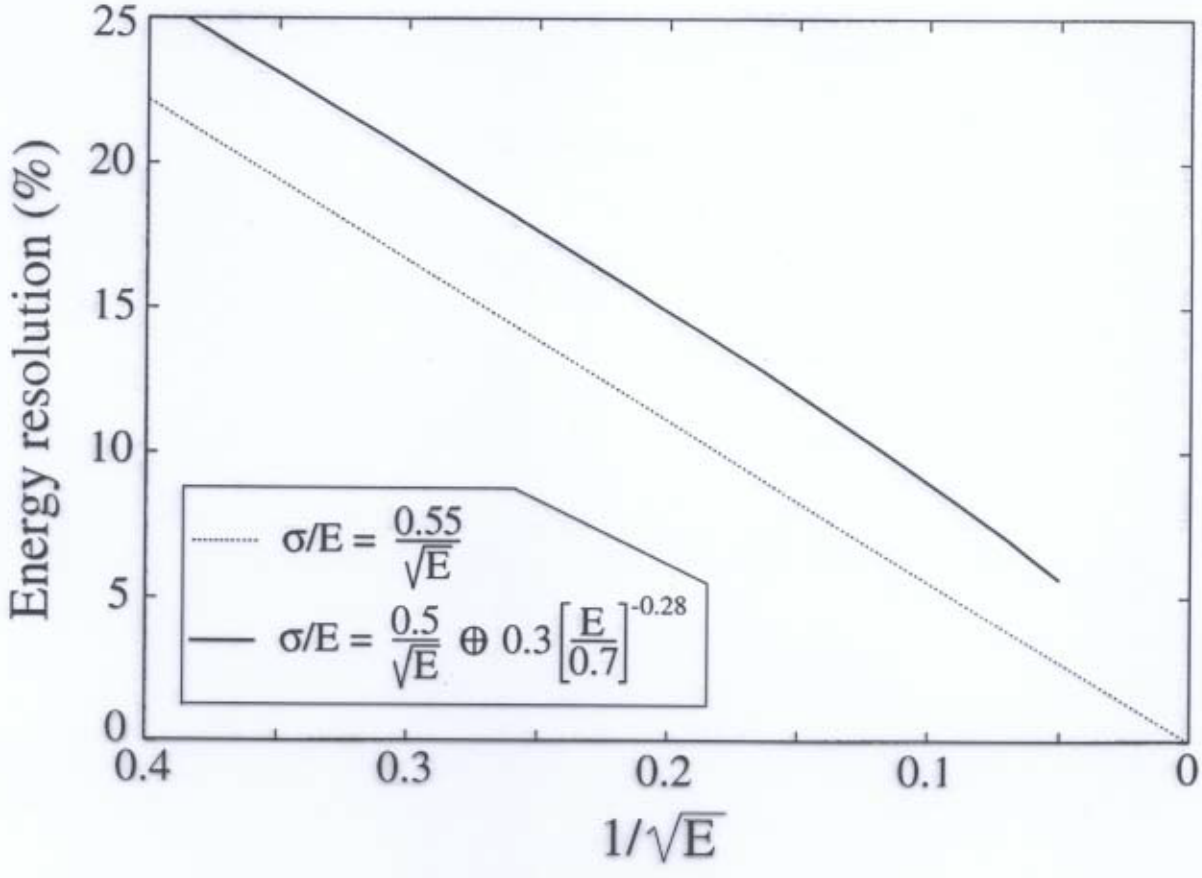

FIG. 4.48. The energy resolution calculated with Equation 4.29 for energies up to 400 GeV (the solid line), and calculated with a sole stochastic term with a slightly larger a_1 value (the dotted line). See text for details.

Compensation in gas calorimeters

Hadronic response function

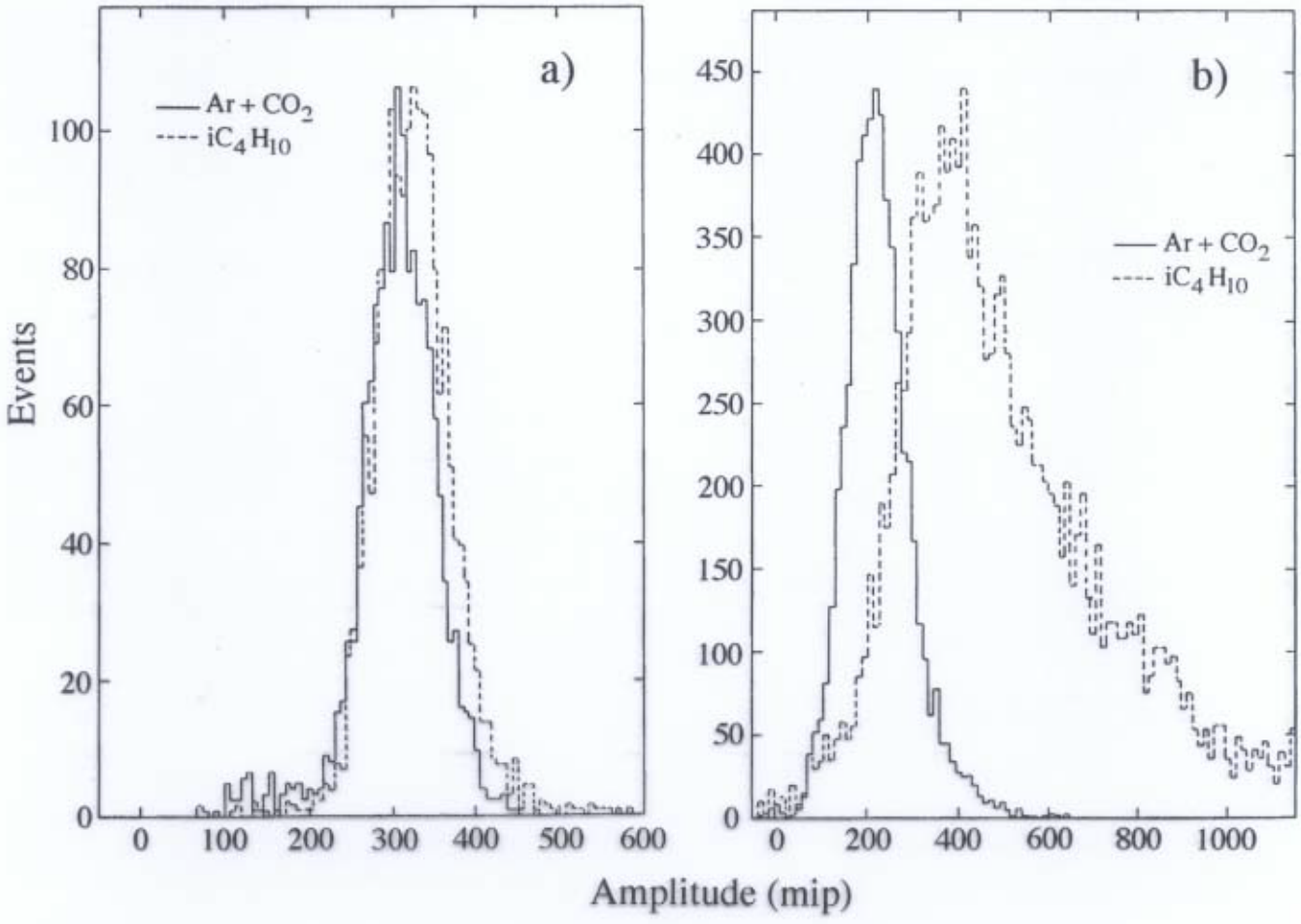

FIG. 4.57. Signal distributions recorded with the L3 ^{238}U/gas calorimeter, for 6 GeV electrons (*a*) and 6 GeV pions (*b*), with two different gas choices. The solid histograms were obtained with a mixture of argon (80%) and CO_2 (20%), the dashed histograms with isobutane [Gal 86].

Dummy compensation

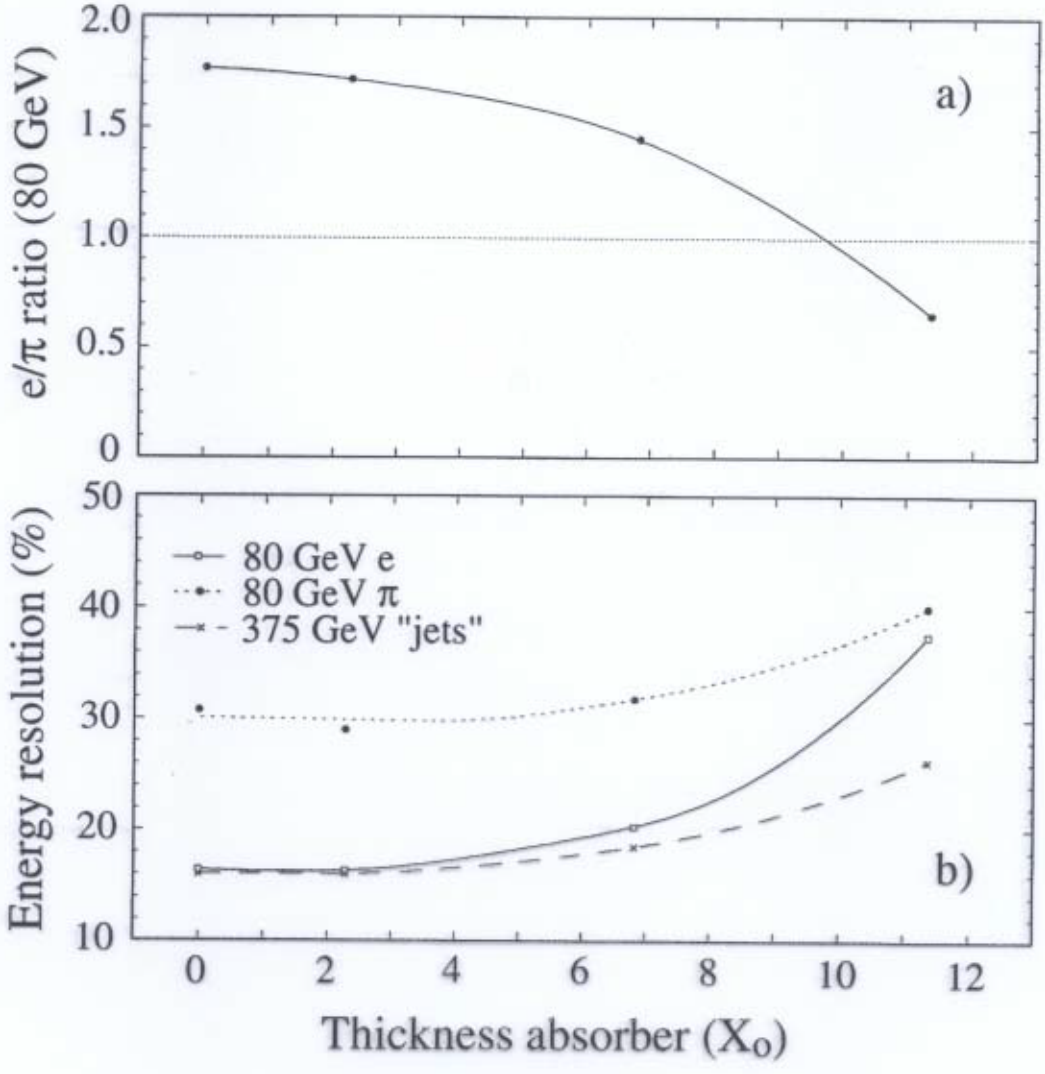

FIG. 4.59. The e/π signal ratio at 80 GeV (a) and the energy resolution (b) of a quartz-fiber calorimeter preceded by dead material (iron), as a function of the thickness of this material [Fer 97]. The energy resolution is given for 80 GeV electrons and pions, and for multi-particle "jets" generated by 375 GeV pions in an upstream target.

Calibration

- Performance of calorimeters determined by processes that take place in the last stages of the shower development (MeV/keV/eV level)

- This has important consequences for calibration of *longitudinally segmented* devices

- The sampling fraction is a function of *depth* (or shower age).
  Example: in em showers, soft γs are sampled differently than mips.
  $\rightarrow$ Ratio (energy deposit/resulting signal) is function of depth.
  Effect is *energy dependent* as well.

- Calibration methods based on minimizing total width are affected:
  - Calibration constants are energy dependent
  - Response non-linearity is introduced
  - Systematic mismeasurement of energy
    (*e.g.*, π^0, e and γ of same energy give different measurement results)

- Effects are even worse for hadrons.
  - Reconstructed energy depends on starting point of shower
  - If calorimeter is calibrated with pions, jet energies are systematically mismeasured

- Resolution is not only determined by the width of a signal distribution, it is also necessary that the distribution is centered around the correct value

- For purposes of energy measurement, a non-segmented calorimeter is preferable

Depth dependent sampling fraction (em showers)

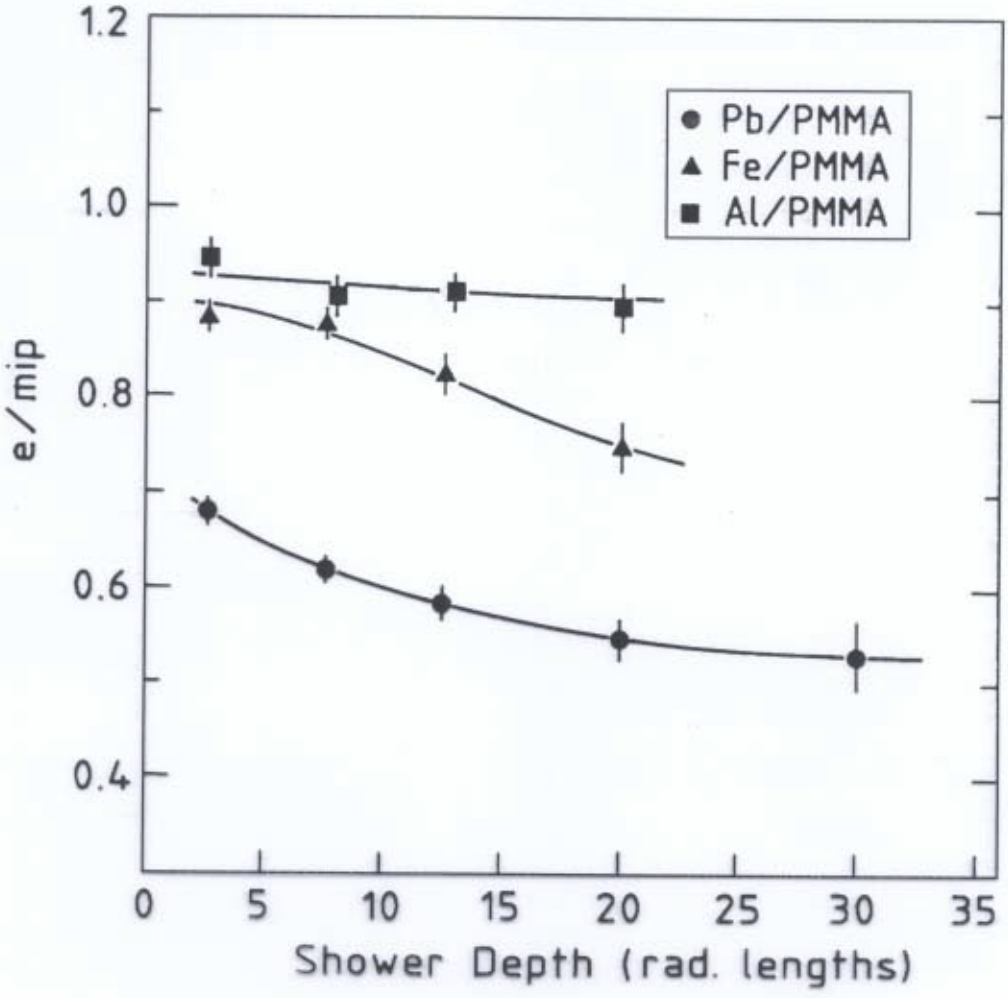

FIG. 3.8. The e/mip ratio as a function of the shower depth, or age, for 1 GeV electrons in various sampling calorimeter configurations. All calorimeters consist of 1 X_0 thick absorber layers, interleaved with 2.5 mm thick PMMA or LAr layers. Results from EGS4 Monte Carlo simulations [Wig 87].

Energy mismeasurement in longitudinal segmented calorimeter (em)

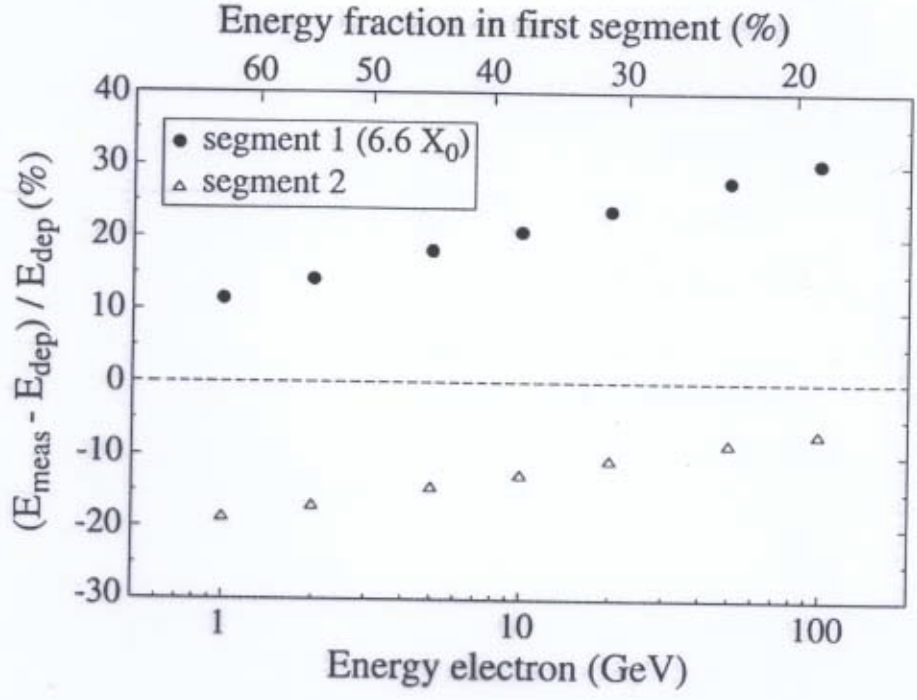

FIG. 6.3. Fractional mismeasurement of the energy deposited in the individual sections of a longitudinally segmented uranium/plastic-scintillator calorimeter, as a function of the energy of the showering electrons (bottom axis) or the energy sharing between the two calorimeter sections (top axis). The energy in the first, $6.6X_0$ deep section is systematically overestimated, the energy in the second segment is systematically underestimated, when the scintillator signals are considered a measure for the deposited energy.

Calibration problems in longitudinally segmented calorimeter (em)

The calibration constants A and B for the em and hadronic calorimeter sections, respectively, were determined by minimizing the width of the total signal distribution, *i.e.* by minimizing the quantity

$$Q = \sum_{j=1}^{N} \left[E - A \sum_{i=1}^{n} S_{ij}^{\mathrm{em}} - B \sum_{i=1}^{n} S_{ij}^{\mathrm{had}} \right]^2 \tag{6.2}$$

where E is the beam energy and $\sum S^{\mathrm{em}}$ and $\sum S^{\mathrm{had}}$ are the sums of all the signals in the towers i of the em and hadronic calorimeter sections that contributed to the measured signal for event j. With this method, values for A and B and, more importantly, for the intercalibration constant B/A were determined for each calorimeter tower.

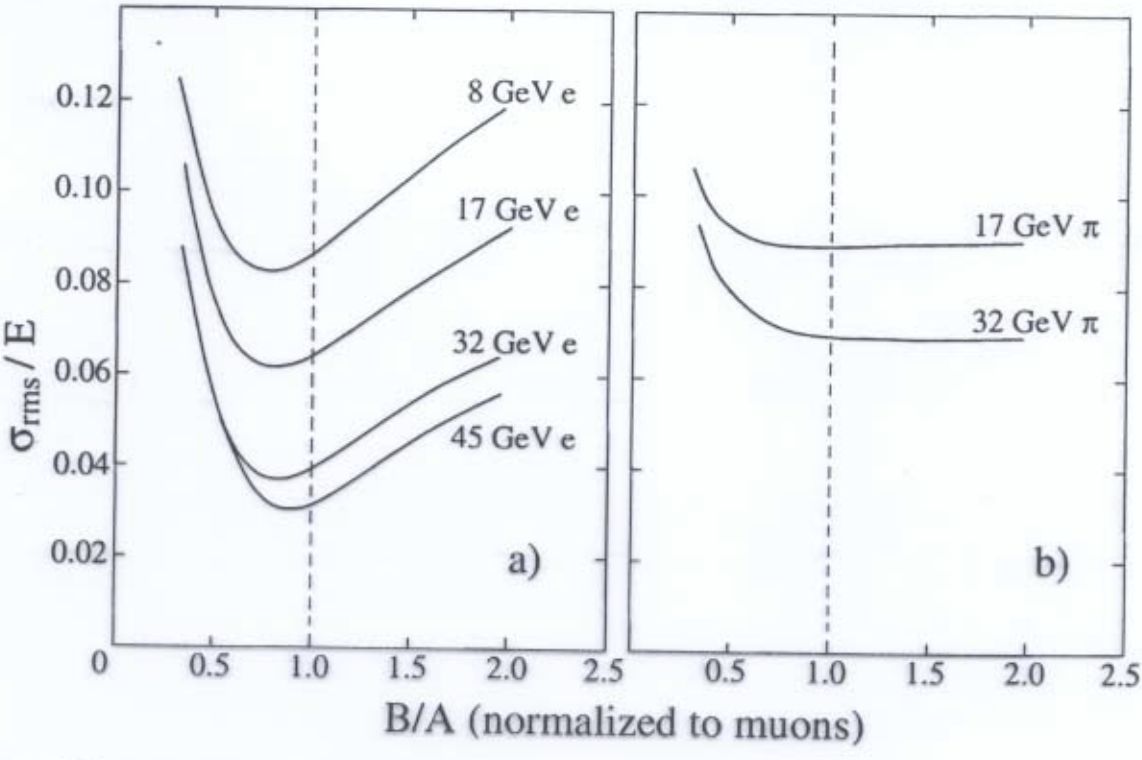

FIG. 6.2. The fractional width σ/E of the signal distributions for electrons (a) and pions (b) of different energies, as a function of the value of the intercalibration constant B/A of the HELIOS calorimeter system. The dashed line corresponds to the intercalibration constant derived from muon measurements [Ake 87].

Čerenkov calorimetry

- Active materials only sensitive to *relativistic* shower particles:
  Water, leadglass, quartz (fibers)

- Čerenkov light *directional* $\rightarrow$ angular dependence of response

- Hadron showers: Only sensitive to em shower component
  $\rightarrow$ ultimate non-compensating calorimeter ($e/h \approx 7$)
  Consequences:
  - Narrow shower profiles
  - Instantaneous response

- Interesting application: *Dual-readout calorimetry*

  dE/dx and Č light provide *complimentary* information.

  May be used to determine f_{em} *event-by-event*

  $\rightarrow$ Limited-mass calorimetry, compensation in small volume, *etc.*

  See talk by V. Nagaslaev

Angular response of fiber calorimeters

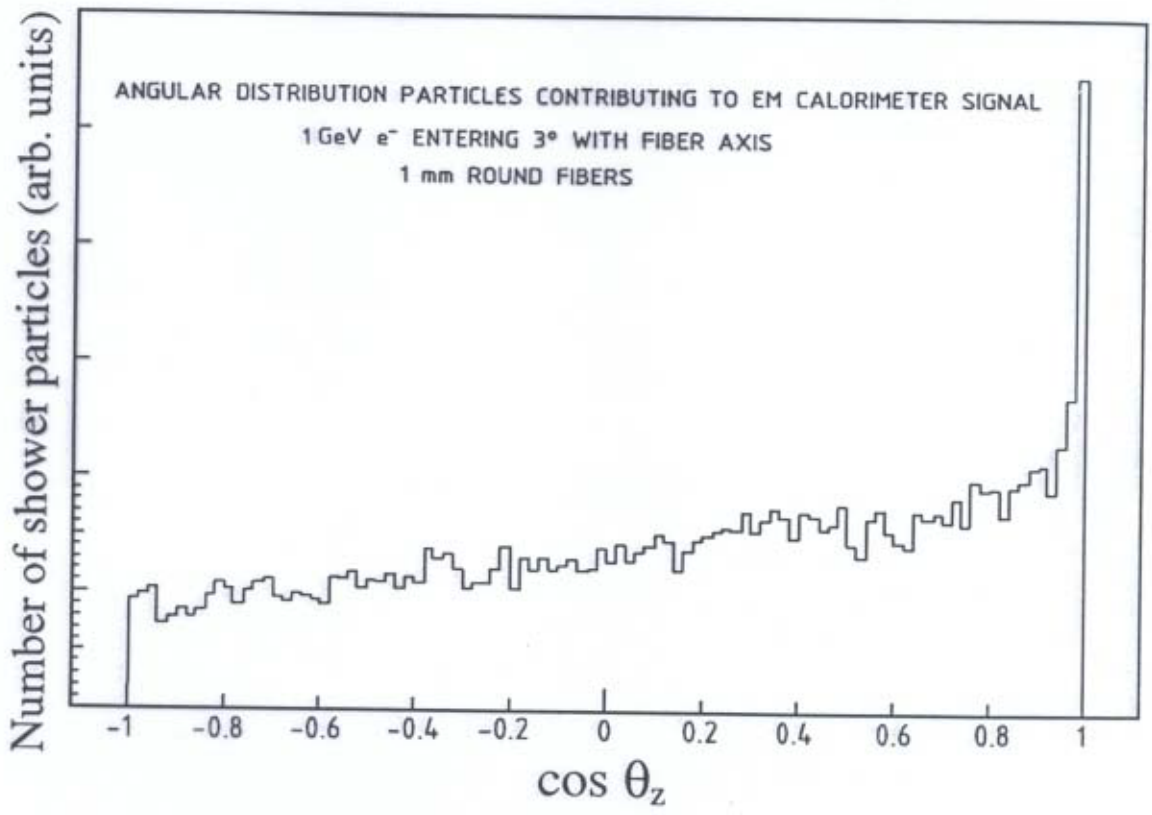

FIG. 2.39. Angular distribution of the shower particles (electrons and positrons) through which the energy of a 1 GeV electron is absorbed in a lead-based calorimeter. Results of EGS4 Monte Carlo simulations. From [Aco 90].

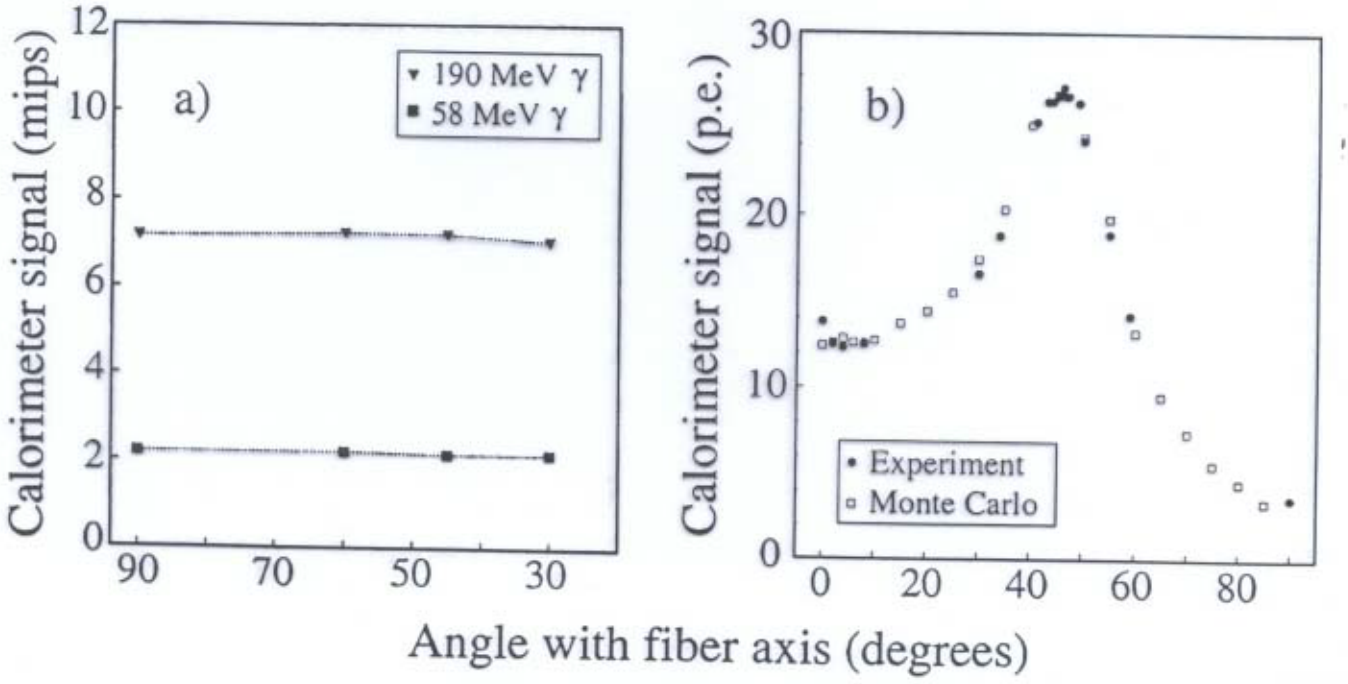

FIG. 3.37. The electromagnetic calorimeter response in fiber calorimeters based on the detection of scintillation light (*a*) or Čerenkov light (*b*), as a function of the angle of incidence of

Lateral hadronic shower profiles

$\left(\frac{dE}{dx} \text{ vs } \check{C}\right)$

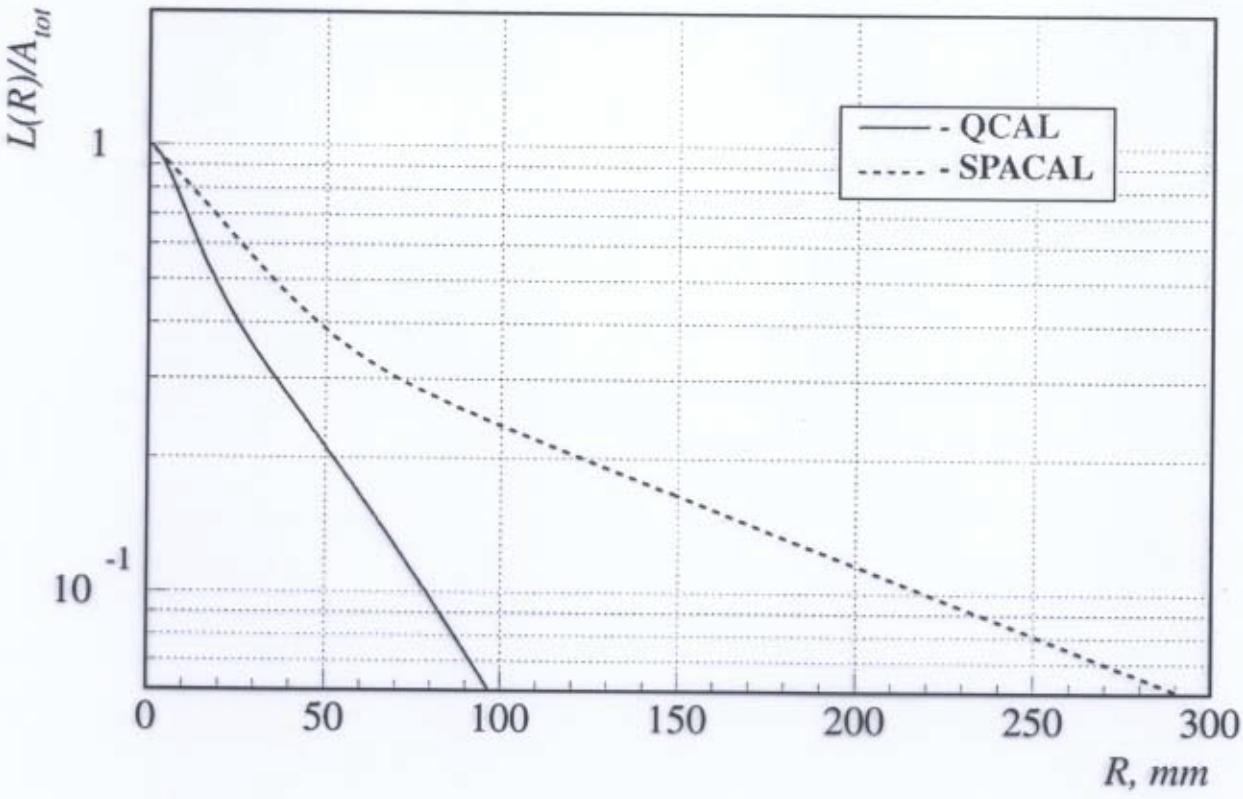

FIG. 2.36. A comparison of the transverse characteristics of 80 GeV π^- showers measured with a scintillation calorimeter [Aco 92b] and with a Čerenkov calorimeter [Akc 97]. Shown is the fraction of the signal recorded outside a cylinder with radius R around the shower axis, as a function of R.

Signal speed of Č calorimeters

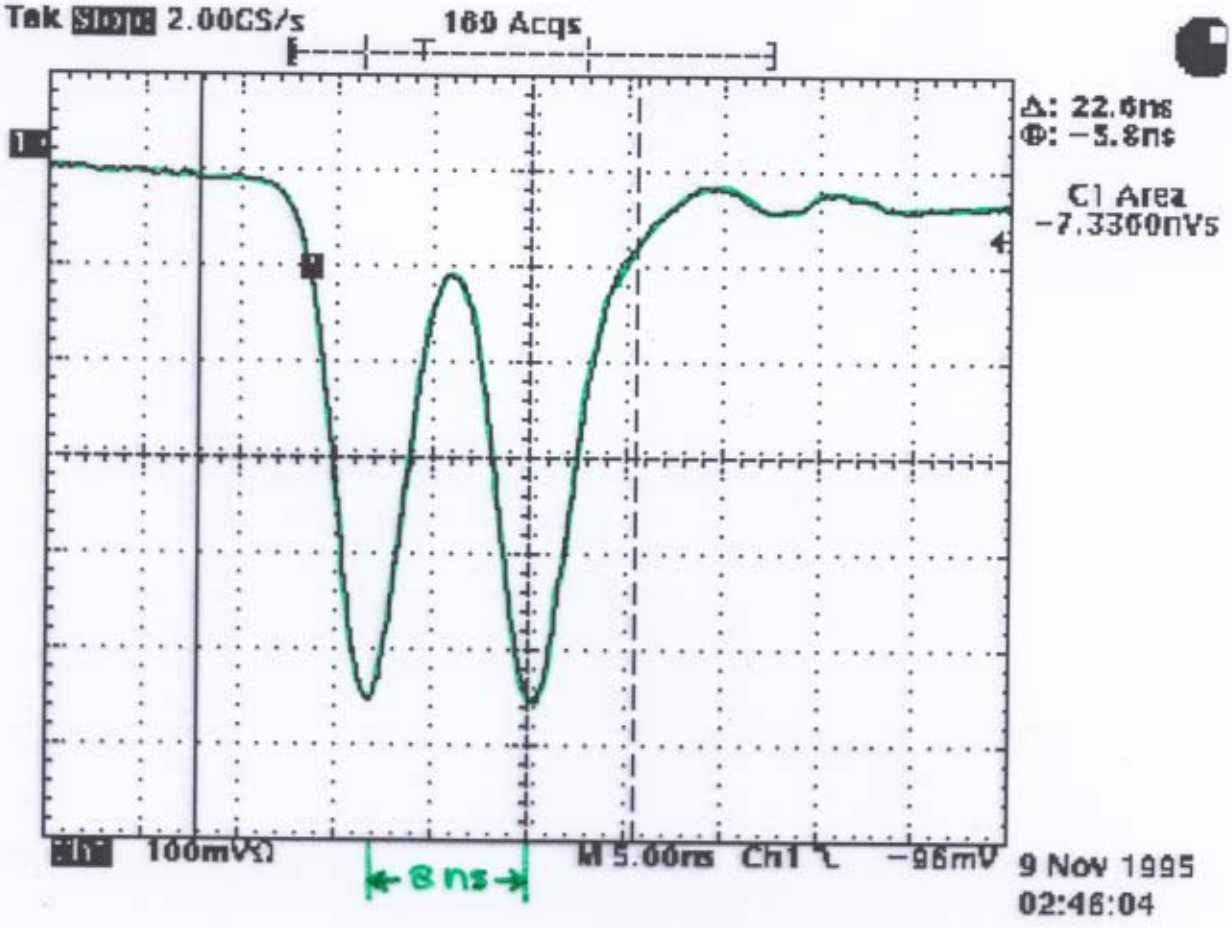

FIG. 7.19. Oscilloscope picture of two events separated by 8 ns in the Zero Degree Quartz Fiber Calorimeter of the NA50 experiment in the CERN heavy-ion beam [Arn 98].

e/π separation on the basis of time structure calorimeter signals

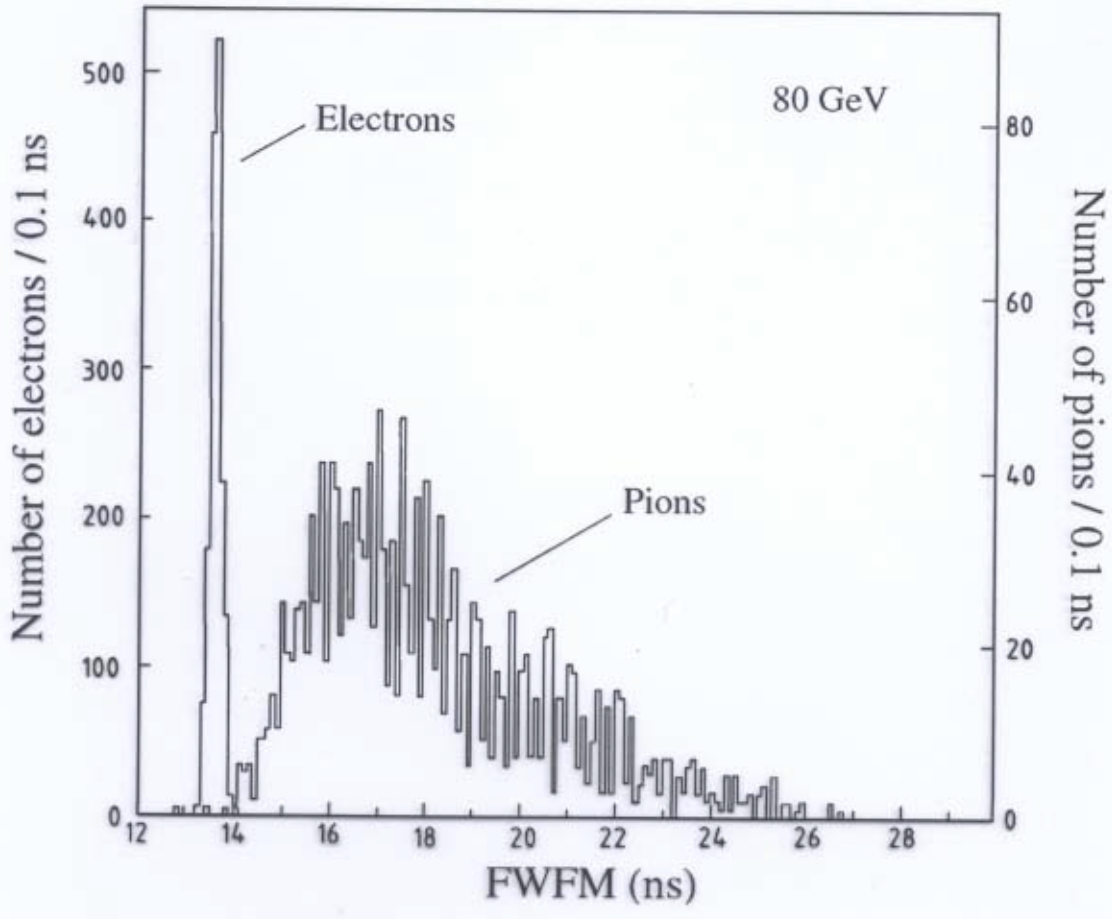

FIG. 7.33. The distribution of the full width at one-fifth maximum (FWFM) for 80 GeV electron and pion signals in SPACAL [Aco 91a]. The left-hand scale applies to the electron signals, the right-hand scale to the pion signals.

Dual-readout calorimetry

Q/S ratio measures leakage event-by-event

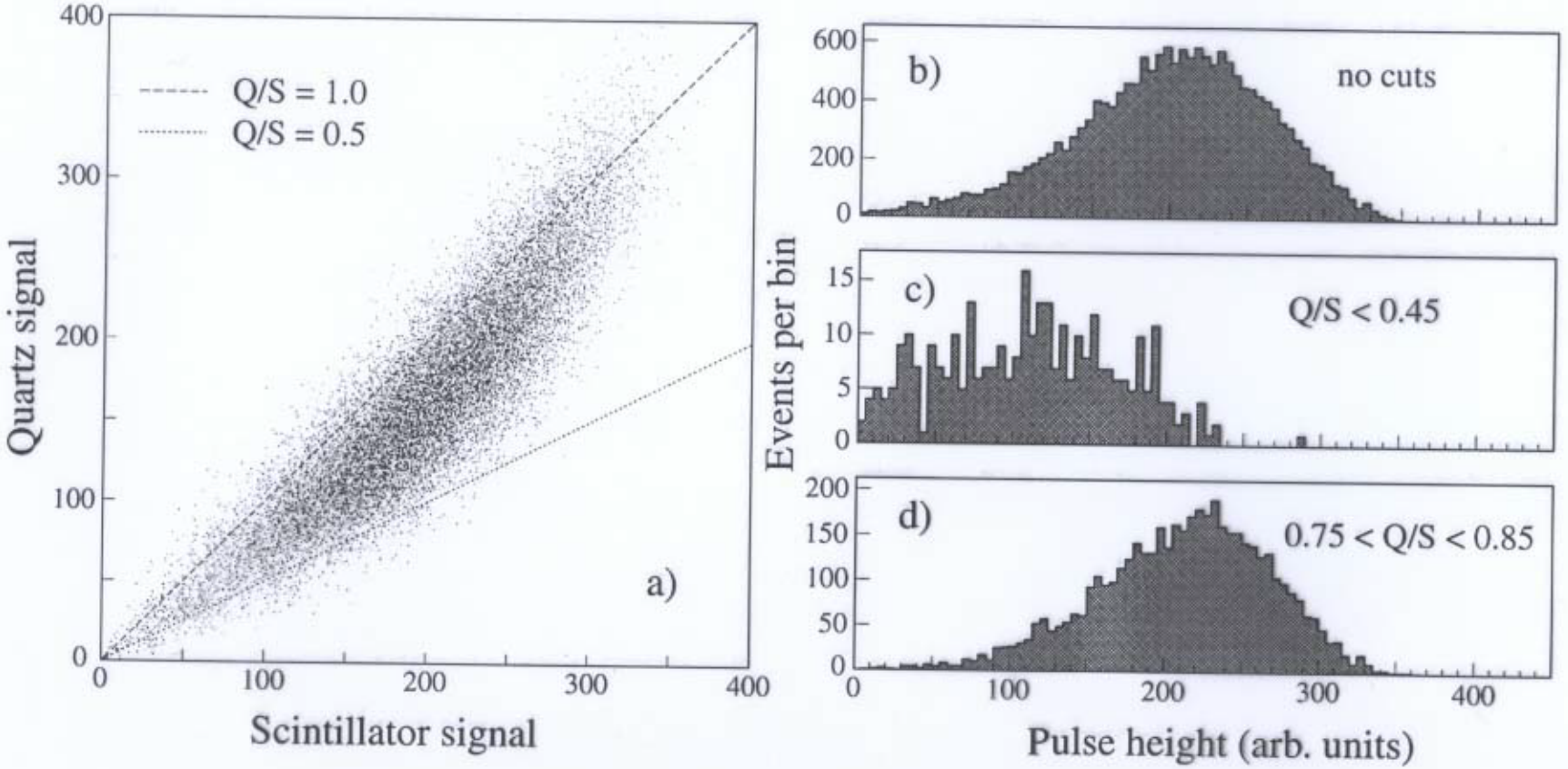

FIG. 8.30. Results of tests of the dual-readout ACCESS calorimeter with 375 GeV pions. Scatter plot of the signals recorded in the quartz fibers *vs.* those in the scintillating fibers (*a*). The signal distributions from the scintillating fibers for all events (*b*) and for subsets of events with a small (*c*) or average (*d*) fraction of Čerenkov light [Nag 99].

Monte Carlo simulations and calorimetry

- **Electromagnetic calorimetry**

  EGS4 highly reliable → learned a lot of important things

  - Origin of $e/mip \neq 1$, Z-dependence of effect
  - Detailed understanding of sampling fluctuations
  - Cause of depth dependence of sampling fraction
  - Angular response dependence of fiber calorimeters
  - *etc.*

- **Hadron calorimetry**

  GEANT/GEISHA/FLUKA .... have not contributed *anything* to our fundamental understanding of hadron calorimetry

  Progress in understanding has been made *in spite of* these programs

  Simulations are *flawed at fundamental levels*, *e.g.* π^0 production and neutron contributions to the signals, which are crucial for understanding hadron calorimetry

  Benchmark data for tests of MC simulations:

  - E. Bernardi *et al.*, NIM **A262** (1987) 229
  - G. d'Agostini *et al.*, NIM **A274** (1989) 134
  - N. Akchurin *et al.*, NIM **A408** (1998) 380.

Benchmark data for hadronic MC

test of π^0 production modelling

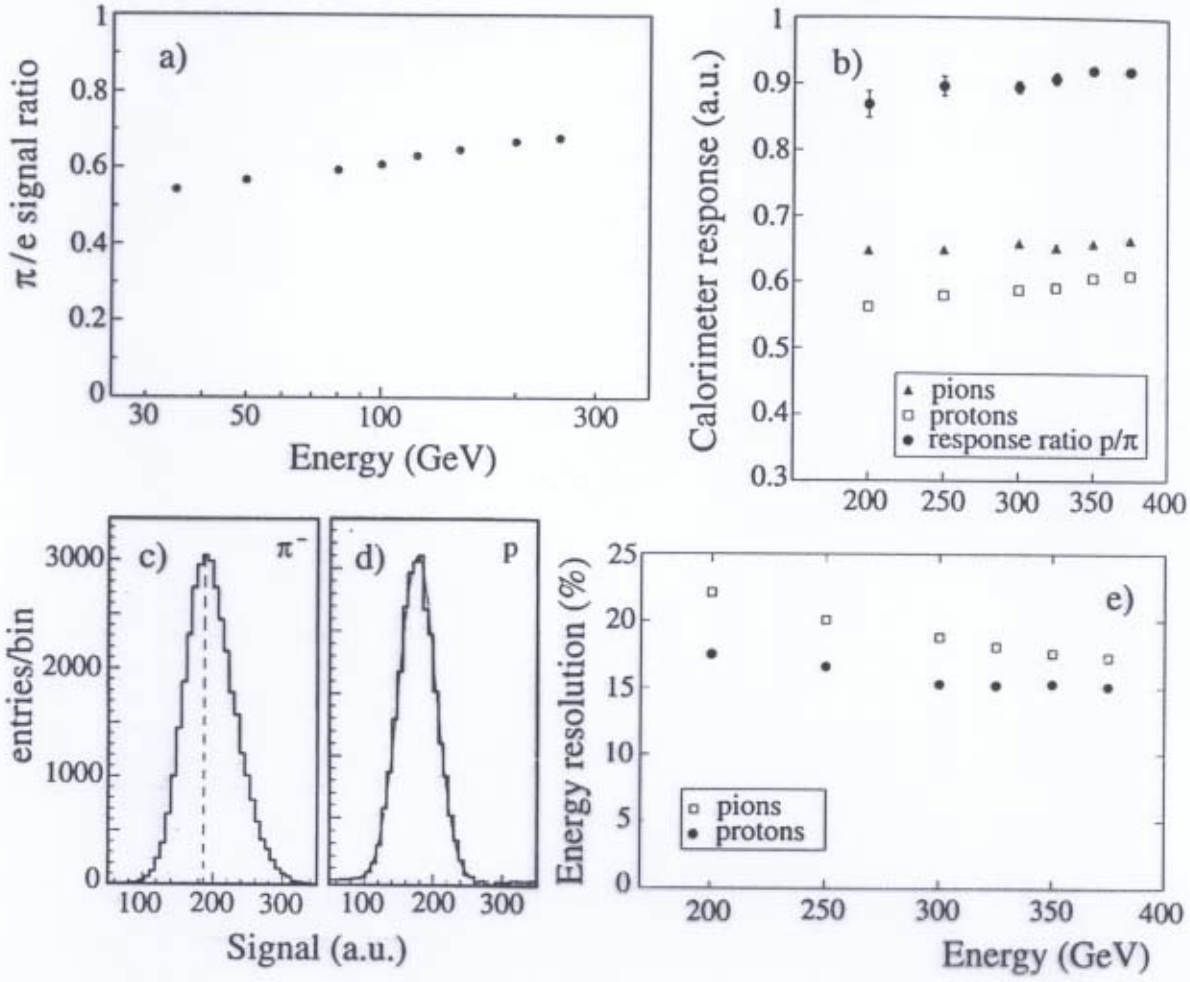

FIG. 8.27. Calorimeter benchmark data for testing the correct implementation of π^0 production in Monte Carlo simulations of hadronic shower development. Experimental data from a copper/quartz-fiber calorimeter, showing the π/e signal ratio as a function of energy (*a*), the response to protons and pions, as well as the ratio of these responses, as a function of energy (*b*), the response functions to 300 GeV pions (*c*) and protons (*d*), and the energy resolutions for pions and protons as a function of energy (*e*) [Akc 97].

Benchmark data for hadronic MC test of description neutron effects

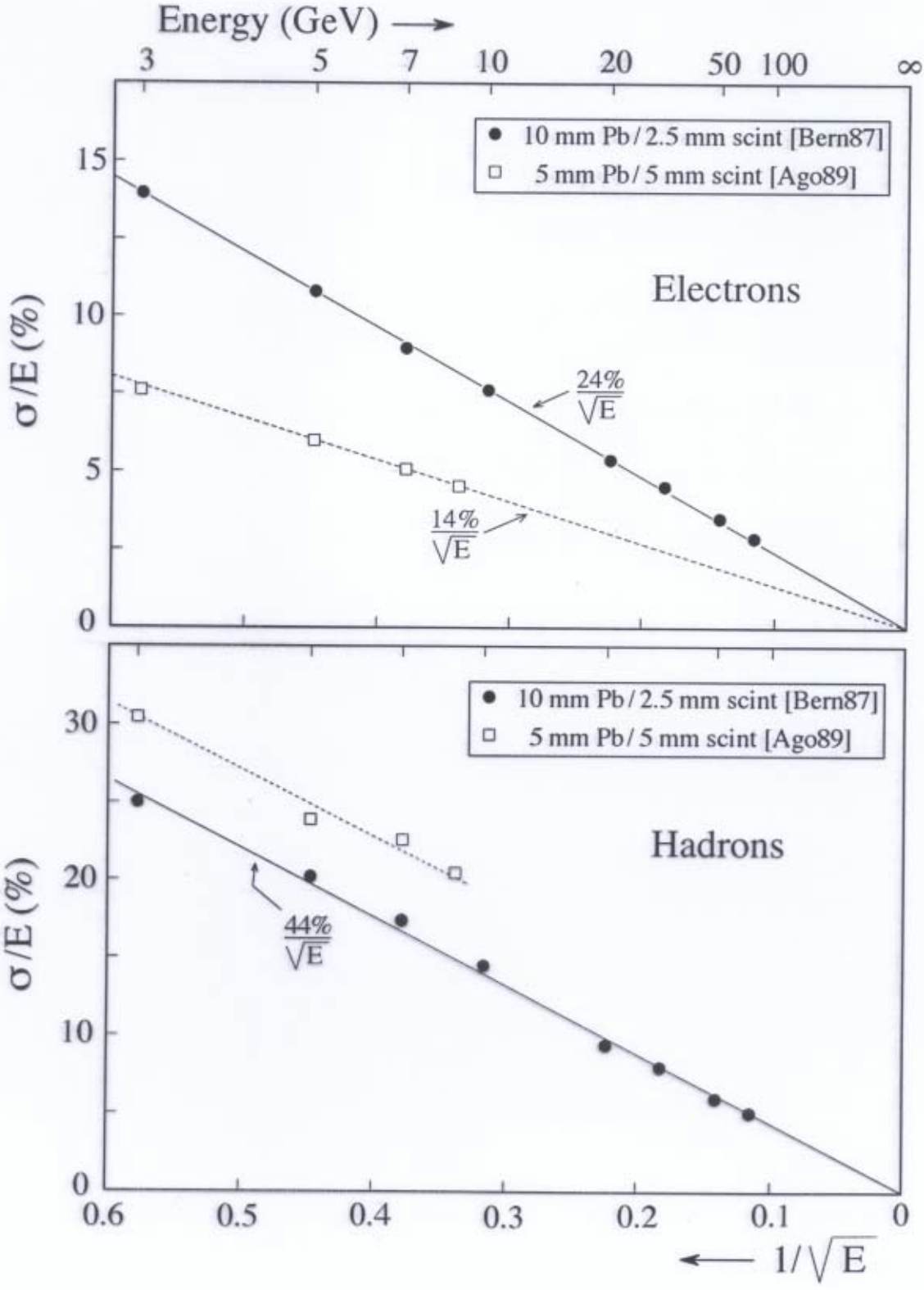

CONCLUSIONS

- Calorimeters are highly non-trivial instruments.
- However, we have come a long way learning the tricks.
- Looking forward to learn a lot of new things this week.